# Oligodendrocyte precursor cells stop sensory axons regenerating into the spinal cord

Hyukmin Kim,[1] Andy Skuba,[1] Jingsheng Xia,[2] Sung Baek Han,[1] Jinbin Zhai,[1] Huijuan Hu,[2] Shin H. Kang,[1] and Young-Jin Son[1]*

[1]Department of Neural Sciences, Shriners Hospitals Pediatric Research Center, Lewis Katz School of Medicine, Temple University, Philadelphia, PA
[2]Department of Medicine, New Jersey Medical School, Rutgers University, Newark, NJ

* Corresponding author. Email: yson@temple.edu

## SUMMARY

Primary sensory axons stop regenerating as they re-enter the spinal cord, resulting in incurable sensory loss. What arrests them has remained unclear. We previously showed that axons stop by forming synaptic contacts with unknown non-neuronal cells. Here, we identified these cells in adult mice as oligodendrocyte precursor cells (OPCs). We also found that only a few axons stop regenerating by forming dystrophic endings, exclusively at the CNS:PNS borderline where OPCs are absent. Most axons stop in contacts with a dense network of OPC processes. Live imaging, immuno-EM and OPC-DRG co-culture additionally suggest that axons are rapidly immobilized by forming synapses with OPCs. Genetic OPC ablation enables many axons to continue regenerating deep into the spinal cord. We propose that sensory axons stop regenerating by encountering OPCs that induce presynaptic differentiation. Our findings identify OPCs as a major regenerative barrier that prevents intraspinal restoration of sensory circuits following spinal root injury.

## KEYWORDS

brachial plexus injury, dorsal root entry zone, dorsal root injury, DREZ, diphtheria toxin A, NG2 glia, oligodendrocyte progenitor cells, PDGFRα, retraction bulb, spinal cord regeneration

## INTRODUCTION

The dorsal root (DR) carries primary sensory axons projecting centrally from DR ganglia (DRG). DR injuries, which commonly result from brachial plexus trauma, cause incurable loss of sensation, motor incoordination and chronic pain [1]. The devastating consequences are because DR axons stop regenerating at the entrance of the spinal cord, the dorsal root entry zone (DREZ), and therefore fail to restore connections with intraspinal neurons. Both neuron-intrinsic and -extrinsic mechanisms, which limit axon regrowth elsewhere in the CNS [2-4], are believed to prevent re-entry of DR axons. Unlike spinal cord injury, DR cut or crush injury damages axons in the PNS without causing an impassable glia scar at the DREZ. Nevertheless, DR axons stop at the scar-free DREZ, even after a nerve conditioning lesion that boosts regenerative ability of DRG neurons [5,6].

How the scar-free DREZ or spinal cord stops axons remains unclear, but myelin-associated inhibitors (MAIs) and chondroitin sulfate proteoglycans (CSPGs) are conventionally considered responsible [7,8]. Surprisingly, however, co-eliminating MAIs (Nogo/Reticulon-4, MAG, OMgp) and CSPGs enables only a few conditioning-lesioned axons to extend a short distance beyond the DREZ [9]. These findings led us to speculate that unknown mechanism(s), unrelated to MAIs and CSPGs, may primarily account for the vigorous arrest of DR axons at the DREZ.

Our earlier findings also challenged the notion that DR axons stop by forming dystrophic endings or retraction bulbs [7], like severed CNS axons degenerating after spinal cord injury [10,11]. This prevalent notion was based on the large bulbous endings occasionally reported in light- or ultramicroscopic studies. The first *in vivo* imaging of regenerating DR axons, however, revealed that axons rapidly stop at the DREZ and remain completely immobilized, with only a few enlarging their tips to resemble dystrophic endings. Furthermore, ultrastructural surveys targeting immobilized axons disclosed synapse-like or apparent presynaptic endings that formed on unknown non-neuronal cells [6]. These findings led us to suggest that unknown non-neuronal cells stop regenerating axons by eliciting presynaptic differentiation [6,12].

Here, we report that these non-neuronal, postsynaptic cells are oligodendrocyte precursor cells (OPCs), also known as NG2 glia, that form bona fide synapses with unmyelinated axons widely in the adult CNS [13-15]. Additionally, we suggest that OPCs may play a more decisive role than other extrinsic mechanisms, and that dystrophic endings form infrequently in the absence of OPC contacts. These findings provide new insights into the regeneration failure of sensory axons at and beyond the DREZ, and the pathophysiological significance of OPCs in the traumatized nervous system.

## RESULTS

### Only a few axons stop by forming dystrophic endings exclusively at the borderline

Most DR axons do not stop regenerating at the CNS:PNS glia borderline where astrocytes/oligodendrocytes are tightly juxtaposed to Schwann cells. They cross the borderline and then stop at the DREZ, which is a region of CNS tissue that extends for ~100μm beyond the borderline (see Figure 3C) [6,9]. Because we did not observe retraction bulbs or dystrophic endings, we extended our earlier work by expanding ultrastructural surveys to look for the formation of these endings in a broader area of the DREZ.

We crushed cervical roots of adult mice and prepared serial longitudinal slices of dorsal spinal cord containing a root at 2 wpi. These preparations facilitated distinguishing CNS and PNS territory across the borderline under electron microscopy (EM; e.g., Figure 5C). Consistent with our earlier work, we frequently observed synapse-like contacts at the DREZ that appeared to form on non-neuronal cells (Figure 1A). In contrast, thorough searches of wide areas on numerous slices only occasionally revealed large bulbous, disorganized axon endings. These endings were 3 to 5 times larger than axons and densely filled with disorganized multi-organelles and scattered vacuoles (Figure 1B). Notably, dystrophic endings were usually observed at the borderline, but not in deeper CNS territory of the DREZ. Furthermore, unlike synapse-like contacts, these large endings were embedded in collagen fibers and displayed a noteworthy absence of cellular contacts (Figure 1B). Similarly, we noted that dystrophic endings described by previous authors also lacked cellular contacts and were observed in PNS territory beyond the DREZ [5].

We next employed light microscopic approaches to examine the incidence and location of dystrophic endings. In the first, we selectively labeled regenerating axons by microinjecting AAV2-GFP into DRGs after crushing cervical roots and assessed them in serial transverse sections at 2 wpi (Figure 1C). Some sections displayed large bulbous, presumptive dystrophic, endings, which represented ~5% axons. Consistent with ultrastructural surveys, these endings were observed close to the borderline, but not deep in the CNS territory. Our second approach was to examine DR axons in their entirety without sectioning. To do this, we performed Clarity tissue clearing at 2 wpi, and examined fluorescently labeled axons in an entire root prepared in wholemounts (Figure 1D). High resolution 3D imaging of cleared roots revealed a small number of parent axons that turned around or formed dystrophic endings near the borderline. These axons represented ~15% and ~10% of all GFP+ axons, respectively. In contrast, most axons extended further and then stopped by forming small endings and frequent swellings on their shafts resembling axonal varicosities. Collectively, together with our earlier data, these findings show that DR axons stop by forming synapse-like contacts or dystrophic endings. They also suggest that dystrophic endings are formed at the borderline by occasional axons entrapped in collagen fibers, unlike synapse-like contacts formed by many other axons making cellular contacts after crossing the borderline.

**Two-photon imaging confirms rapid axon immobilization at the DREZ**

In contrast to the prevailing view, these data suggest that only a few axons stop by forming dystrophic endings. The conventional view was primarily based on the observations that DRG axons *in vitro* retract in response to MAIs [16], or stall and become dystrophic when exposed to a gradient of CSPGs [17]. Moreover, these dystrophic endings remain extremely motile at least for several days [17,18]. In contrast, DR axons that we monitored in living mice with widefield microscopy did not retract, but were rapidly immobilized as they entered the DREZ [6]. To ensure that we have not overlooked subtle axon motility, we performed live imaging using high-resolution two-photon microscopy.

For optimal two-photon imaging, it is essential that fluorescent labeling mark only a small number of DR axons [19]. Accordingly, we used the M line of *Thy1* mice (Thy1-M), in which <5% of DRG neurons are YFP+ [20]. Following DR crush, axons penetrate the crush site in a day or two, and then regenerate along the root at a speed of ~1 mm/day [6]. We crushed an L5 root >4

128 mm from the borderline (Figure 2A), to make regenerating axons arrive at the DREZ as early as
129 5 days post-crush. We then screened ~150 mice on the first day of imaging at 4 or 5 dpi, to
130 identify ~20 mice with 1 (or rarely 2) YFP+ axons superficially positioned within the optimum
131 imaging depth (~150μm below the dura; Figure 2B). We then continuously monitored the distal
132 endings of these axons for up to 5 hours. As anticipated, we observed axons at the DREZ at 5
133 dpi, but none at 4 dpi. Notably, no axons moved forward or retracted; all appeared already
134 stopped at the DREZ. Axon tips with either a slender (Figure 2C) or small roundish shape
135 (Figure 2D) exhibited no perceptible motility other than that due to respiration-induced artifacts.
136 No axons noticeably enlarged their tips, forming putative dystrophic endings. Following the first
137 day of imaging, we imaged these axons repeatedly over several days to exclude the possibility
138 that the immobility was due to phototoxicity (data not shown). These findings thus confirm that
139 axons become rapidly immobilized, within a day or likely sooner, at the DREZ *in vivo*.
140
141 **Relative positions of non-neuronal cells and arrested axons at the DREZ**
142 To determine the extrinsic mechanism that rapidly immobilizes axons, we next examined various
143 non-neuronal cells at the DREZ before and after DR crush. At 2 wpi, axons that stopped past the
144 borderline were not associated with Schwann cell processes (Figure 3A, 3B), showing that they
145 invaded CNS territory without leading, growth-supporting Schwann cells (Figure 3C; see also
146 Figure 4A). These axons grew through the region of the DREZ, where astrocytes and
147 oligodendrocytes were profuse, suggesting that these glia cannot rapidly immobilize axons
148 (Figure 3A, 3B). Macrophages were far more numerous peripherally but notably sparse at
149 axotomized DREZ (Figure 3B, Figure S1A), suggesting that growth-collapsing activity of
150 macrophages [21,22] contributes minimally if at all to the axon arrest at the DREZ. Blood vessels,
151 known for guiding axon growth [23], were also sparse along the root and at the DREZ (Figure
152 S1D). Similarly, the two types of perivascular cells associated with blood vessels, pericytes and
153 fibroblasts [i.e., vascular leptomeningeal cells (VLMCs)], were also scarce at both intact and
154 axotomized DREZ (Figure S1B, S1D). These perivascular cells remained in association with the
155 blood vessels after DR crush injury (Figure S1C), and we did not observe fibrotic scars filled
156 with numerous macrophages, pericytes and fibroblast-like cells (Figure S1A, S1B), such as those
157 elicited by spinal cord injury [24] or by severe root avulsion (Figure S1D). Because many axons are
158 arrested at the DREZ, it is unlikely that non-neuronal cells that are sparse in the region can
159 account for the rapid arrest of many axons (Figure 3C).
160
161 Interestingly, NG2 staining showed that OPCs and their processes were absent at and within
162 ~50μm of the borderline, but abundant deeper in CNS territory (Figure 3D, 3E; Figure S2A-C).
163 This distribution of resident OPCs before DR injury was consistent in all mice (n >20) and is
164 noteworthy because many axons grow across the borderline and then stop deeper at the DREZ [9].
165 OPCs are defined by their expression of both NG2 and PDGFRα, which are also expressed by
166 other cell types [24,25]. After DR injury, however, almost if not all macrophages were NG2- (Figure
167 S1A). Both VLMCs and meningeal fibroblasts, which express PDGFRα but little if any NG2
168 [26,27], were immunostained weakly if at all by NG2 (Figure S1B). Schwann cells increased NG2
169 expression after injury, but they did not invade the DREZ (Figure 3). NG2+ pericytes, which do
170 not express PDGFRα [26], were also sparse at the DREZ (Figure S1C). Furthermore, the
171 perivascular configuration of pericytes was readily distinguished from the highly ramified
172 morphology of OPCs (e.g., Figure 3D). Lastly, NG2 staining overlapped closely with
173 PDGFRα staining at the DREZ (Figure S1B, S1C). Thus, almost all NG2+ cells at the DREZ

were OPCs. Additionally considering that OPCs form synapses with axons, spatial analysis distinguishes OPCs from other non-neuronal cells.

**OPCs proliferate, migrate, and form a dense meshwork of processes after DR injury**

Next, we examined responses of OPCs to DR injury in wholemounts, which permits comprehensive analysis of an entire root. We used Thy1-H mice in which subsets of degenerating or regenerating YFP+ axons are fluorescently labeled. In intact DRs, OPCs and their ramified processes were intraspinally distributed in a tile-like arrangement but were rare at the borderline (Figure S2A). At 2 wpi, many more OPCs formed a much denser meshwork of processes along the trajectory of degenerating distal axons (Figure S2B). OPC processes were now present at the borderline but remained relatively rare, compared to their density deeper in CNS territory. Also notable was an upregulated expression of NG2 proteoglycans in the PNS, presumably associated with denervated Schwann cells [28] and some fibroblasts [29]. Schwann cell-associated NG2 staining did not preclude identification of OPC processes at the DREZ, however, because it was tube-like and distinctly brighter than that associated with OPCs, which was highly ramified and directionless (e.g., Figure 4A). Temporal analysis in transverse sections showed that by 5 dpi, when DR axons stop at the DREZ, OPC processes had migrated closer to the borderline, and by 2 wpi, their density deeper in CNS territory had increased (Figure S2C). OPCs also rapidly proliferated in response to the distant root injury; their proliferation peaked at 3 dpi, and their number doubled by 1 wpi (Figure S2D). These data suggest that most axons cross the borderline when OPCs are absent and then encounter OPCs.

**Stopped axons without dystrophic endings display extensive contacts with OPC processes**

To determine if stopped axons are associated with OPCs, we labeled regenerating axons with an adeno-associated viral tracer, AAV2-GFP, and examined all detectable axon tips of entire roots in wholemounts at 2 wpi. Distal ends of almost all stopped axons were associated with a dense meshwork of OPC processes which made extensive contacts with axon endings and adjacent shafts (Figure 4A; n > 400 axons, 3 roots). Transverse sections also showed that all axons that crossed the borderline and stopped in CNS territory were in direct contact with OPC processes (Figure 4B). However, dystrophic endings at the borderline were not associated with OPCs (Figure 4B; n= >10). This finding is consistent with the absence of OPCs at the borderline and the lack of cellular contacts by dystrophic endings. These data suggest that axons occasionally stop by forming dystrophic endings embedded in collagen fibers at the borderline where OPCs are absent, whereas many others cross the borderline and then stop by making extensive contacts with OPCs.

**Stopped axons make synaptic contacts with OPC processes at the DREZ**

Next, we used immunolabeling for synaptic markers to determine whether axon-OPC contacts are synaptic. Consistent with the ultrastructural observation of aggregated synaptic vesicles (Figure 1A), a synaptic vesicle marker, SV2, brightly labeled small swellings of axon tips and shafts tightly associated with OPC processes, when assessed in wholemounts at 2 wpi (Figure 5A, 5B). However, although less brightly, SV2 also labeled dystrophic endings and axon swellings that showed no obvious OPC contacts. Other vesicle markers, active zone and postsynaptic markers that we tested were also not convincingly selective (data not shown). Our attempts to trans-synaptically label OPCs by intra-DRG injections of pseudorabies or wheat-germ agglutinin (WGA)-expressing viral tracers were unsuccessful. Other investigators have also

failed to provide light microscopic identification of neuron-OPC synapses, an anatomically and functionally weaker synapse than neuron-neuron synapses [30,31].

To obtain more convincing evidence, we performed immuno-EM. At 2 wpi, we prepared longitudinal slices of dorsal spinal cord containing a root and carefully examined the CNS and PNS areas across the borderline (Figure 5C). In the PNS, gold particles targeted to NG2 proteoglycans selectively labeled Schwann cells but not axons, confirming their specificity (Figure 5D). Remarkably, we frequently observed presynaptic profiles exhibiting vesicle clustering and a thin postsynaptic density in direct apposition to gold particles-labeled postsynaptic processes (Figure 5E). We also observed varicosity-like synaptic profiles, filled with numerous vesicles, formed on gold particles-labeled postsynaptic processes that encircled the axons (Figure 5F). Notably, these postsynaptic processes were thinner than axons, and their membranes, but not cytoplasm, were labeled by gold particles, consistent with the transmembrane location of NG2 proteoglycan [32]. Because no other NG2+ cells form bona fide synapses, our immuno-EM identified OPCs as the postsynaptic cells that induce presynaptic differentiation of DR axons.

**OPCs form functional synapses with co-cultured DRG neurons**

Next, we co-cultured OPCs and DRG neurons to determine whether they form functional connections. As DR axons become unable to penetrate the DREZ, ~1 week after birth [33,34], we purified OPCs from spinal cords of p16-p18 mice and co-cultured them with purified DRG neurons from adult mice. >95% pure OPCs at 3 div were labeled specifically by both markers of OPCs, NG2 and PDGFRα. They resembled OPCs *in vivo* by exhibiting a non-overlapping distribution of bushy NG2+ processes (Figure S3A). A few dissociated neurons were then applied sparsely to the cultured OPCs and co-cultured for 5 days in proliferating medium. The DRG neurons extended relatively short axons on OPCs, which continued to proliferate. Of note, DRG axons frequently developed small swellings which were microtubule-deficient but SV2-enriched, a typical feature of presynaptic terminals (Figure S3B). We did not observe a large bulbous ending, reminiscent of dystrophic endings.

To determine whether these putative synaptic contacts were functional, we performed calcium imaging on the fifth day of co-culture. We loaded cultured cells with a fura-2 AM calcium indicator and locally infused 60mM KCL or 1mM glutamate. We observed, however, rapid calcium responses triggered not only from neurons but also from OPCs (data not shown). To specifically stimulate neurons, we applied capsaicin, which selectively depolarizes nociceptive neurons by activating TRPV1 receptors [35]. Capsaicin did not elicit calcium responses in OPCs cultured without neurons (data not shown). Local capsaicin infusion elicited rapid calcium responses in neurons, followed by calcium responses in adjacent OPCs (Figure S3C). The responses in these OPCs were blocked by combined application of CNQX and AP5, antagonists of AMPA/kainate and NMDA receptors, consistent with earlier studies [36,37]. Following washout of the antagonists, capsaicin-stimulation of the same neuron again evoked calcium responses in the same OPCs. These findings are consistent with an earlier study that demonstrated synaptic vesicle recycling and ultrastructural evidence of synaptic contacts in OPC-DRG cocultures [38]. They indicate that OPCs form functional synapses with DRG neurons *in vitro* and reinforce the notion that axons may rapidly stop regenerating by forming synapses with OPCs.

**OPC ablation enables many axons to regenerate into the spinal cord**

Because no OPC-associated synaptogenic inducer has been identified, we could not selectively inhibit synapse formation between OPCs and DR axons. As an alternative, we genetically ablated OPCs to determine whether they stop DR axons reentering spinal cord. OPC ablation *in vivo* has been difficult because they are highly proliferative and subject to tight spatial homeostasis: residual OPCs vigorously repopulate a depleted area [39,40]. We therefore tried several transgenic strategies and diverse ablation paradigms. The best, yet incomplete, strategy was to use the PDGFRα-CreER driver and induce expression of diphtheria toxin subunit A (DTA). As DTA lacks the B subunit required for DT to penetrate membranes, ablation is restricted to cells synthesizing DTA proteins, which elicit apoptotic extirpation [41]. We crossed PDGFRα-CreER and Rosa-DTA mice to generate PDGFRα-DTA mice and identified a 4-hydroxytamoxifen (4-HT) administration paradigm that elicited maximal ablation at 2 wpi (Figure 6A). Consistent with earlier studies that ablated OPCs by expressing DT receptors (DTR) or DTA [42-44], PDGFRα-DTA mice were grossly normal. NG2 and PDGFRα were markedly reduced as assessed by western blotting (Figure 6B) and immunostaining (Figure 6D, S4A). As anticipated, the extent of OPC ablation was quite variable, ranging between 20-80% at 2 wpi, as determined by mean fluorescence intensity of NG2 in the spinal cord. None of the administration regimens that we tried achieved more consistent or complete ablation. We therefore selected mice with at least 60% ablation at 2 wpi for further analysis (Figure 6C).

At 2 wpi, some OPC processes usually remained at the DREZ even in mice with ~80% ablation of OPCs (Figure 6D), presumably reflecting more vigorous proliferation of OPCs along the trajectory of degenerating injured axons. Remarkably, PDGFRα-DTA mice showed a greater number of axons at and beyond the DREZ than control mice (Figure 6D). The number of axons counted peripherally in PDGFRα-DTA mice did not differ from that in control mice, indicating that the enhanced regrowth was not due to an increase in axons regenerating peripherally (Figure 6E). Quantification of GFP+ axons showed that OPC ablation almost tripled the number of axons that extended past the DREZ (Figure 6F). Several considerations make the increase even more noteworthy. First, axons frequently extended unusually deeply, into the dorsal funiculus. Second, AAV2-transduced GFP+ axons are predominantly large-diameter axons whose growth capacity is particularly weak [9], yet even incomplete OPC ablation enabled ~30% of these weak regenerators to cross the DREZ. Indeed, such a large increase rivaled the levels achieved by combining a conditioning lesion with simultaneous removal of myelin inhibitors and CSPGs [9].

**Enhanced regeneration is not due to indirect effects of OPC ablation**

Recent scRNA sequencing studies indicated that PDGFRα is also expressed in VLMCs and that NG2 is also expressed in pericytes [26,45,46]. This suggests that VLMCs and other PDGFRα+ fibroblasts are also deleted in PDGFRα-DTA mice. Additionally, NG2 staining will label OPCs and pericytes, whereas PDGFRα staining will label OPCs and VLMCs. Consistent with this notion, vascular NG2+/PDGFRα- labeling remains in PDGFRα-DTA mice, indicating that pericytes are not deleted (Figure S4A). PDGFRβ staining, which labels both pericytes and VLMCs, was reduced in PDGFRα-DTA mice, reflecting ablation of VLMCs (Figure S4B). In the PNS of uninjured control mice, we observed PDGFRα+ cells diffusely scattered between nerve fibers; these cells were not Schwann cells (Figure S4C), but were endoneurial fibroblasts (Figure S4D). PDGFα staining was markedly increased in the DR after root crush, reflecting rapid proliferation of endoneurial fibroblasts [29]. We did not, however, observe a significant

312 difference in root-associated PDGFRα staining between control and PDGFRα-DTA mice after
313 injury (Figure S4D). Together, these data suggest that some PDGFRα+ fibroblasts are
314 additionally deleted in PDGFRα-DTA mice. Their ablation, however, is highly unlikely to
315 account for the enhanced regeneration, because VLMCs are sparse at intact and axotomized
316 DREZ (Figure S1), and because axons regenerated normally along the roots in PDGFRα-DTA
317 mice (Figure 6E).
318
319 Apoptosis does not induce an inflammatory response [47,48]. In accordance, and consistent with
320 earlier studies of OPC ablation [42,49,50], the inflammatory responses of PDGFRα-DTA mice were
321 comparable to those of control mice: the morphology, distribution, and numbers of microglia and
322 macrophages in the spinal cord and DRs were not significantly different (Figure S5A-B, S5D-F).
323 Astrocytes, which inhibit Schwann cell migration [51], also showed no differences in morphology,
324 density, or reactivity (Figure S5C, S5G). NG2 staining in the PNS of PDGFRα-DTA mice was
325 slightly diminished, as compared to control mice, at 2 wpi (Figure S6A, S6E). Because Schwann
326 cells do not express PDGFRα mRNAs [52], this reduction likely reflects ablation of some
327 PDGFRα+ endoneurial fibroblasts. Consistent with this notion and Figure S4C, the density and
328 reactivity of Schwann cells in DTA and control mice were not significantly different (Figure
329 S6B-C, S6F-G). Lastly, NG2, also known as CSPG4, is a constituent of growth inhibiting
330 CSPGs [2,53]. It is conceivable, therefore, that a reduction of NG2/CSPG4 is the basis of enhanced
331 regeneration by OPC deletion. We found, however, abundant expression of CSPGs in PDGFRα-
332 DTA mice, as indicated by CS56 immunoreactivity (Figure S6D, S6H). Moreover, we were
333 unable to achieve more robust regeneration even after broad removal of all CSPGs [9].
334 Collectively, these data exclude that the enhanced regeneration was due to indirect effects on
335 axons caused by ablating OPCs.
336
337 **Axons continue regenerating intraspinally through areas lacking OPCs**
338 Stopped axons remained remarkably stable at the DREZ for at least 4 months after injury [6]. We
339 also reported that axons remain immobilized for at least 4 weeks at the DREZ, despite
340 simultaneous and prolonged removal of myelin inhibitors and CSPGs [9]. If OPCs play a primary
341 role in stopping axons, then axons may continue to grow with prolonged ablation of OPCs, even
342 in the presence of other extrinsic inhibitors. To test this notion, we examined PDGFRα-DTA
343 mice after longer survival, 4 wpi (Figure 7A). As anticipated, OPCs widely repopulated and re-
344 formed an OPC meshwork in most areas of the spinal cord; their overall densities corresponded
345 to ~70% of those in control mice (Figure 7B). Of note, however, OPC repopulation was not
346 uniform; there were areas in which OPCs remained reduced or sparse (Figure 7D, S7A-B).
347 Consistent with our previous study, in control mice, regeneration across the DREZ did not
348 increase between 2 wpi and 4 wpi (Figure 7D, 7E). In striking contrast, in PDGFRα-DTA mice,
349 GFP+ axons more frequently extended significantly deeper into the dorsal funiculus at 4 wpi
350 than at 2 wpi (Figure 7D, S7A-B) and occasional axons regrew remarkably deeply into the dorsal
351 horn (Figure 7D). Intraspinal growth of DR axons that reached deep layers of the dorsal horn
352 was indeed extraordinary, because it was not achieved even by a nerve conditioning lesion [9] or
353 PTEN deletion (Kim et al, in preparation). Also notable was a conspicuous reduction of OPC
354 processes in areas where more axons grew deeper (Figure 7D). Furthermore, axons that extended
355 through OPC-deficient areas terminated in OPC-rich regions (Figure S7A-B). The number of
356 axons extended from the PNS did not increase (Figure 7C) nor did the number of axons counted
357 at 100μm from the borderline in the CNS (Figure 7E). Therefore, the enhanced regeneration was

358 due to sustained growth of the axons already present at the DREZ at 2 wpi, rather than by axons
359 that freshly crossed the borderline. Taken together, these observations suggest that some axons
360 could continue regenerating into the area of spinal cord where residual or repopulating OPCs
361 were relatively rare.
362
363 **DISCUSSION**
364 Here, we identify OPCs as the postsynaptic cells arresting sensory axons regenerating into the
365 spinal cord. Our studies provide additional insights into the regeneration failure at the DREZ,
366 prompting us to propose a new model (Figure 7F): Regenerating axons exiting basal lamina
367 tubes at the borderline turn around or stop immediately by forming dystrophic endings if their
368 growth is obstructed by collagen fibers. Most axons cross the borderline into CNS territory,
369 albeit extending slowly due to poor regenerative ability, extrinsic growth-inhibitory molecules
370 and lack of leading Schwann cells. These axons stop as they encounter a dense meshwork of
371 OPC processes that induce presynaptic differentiation. Concurrent induction at multiple axon-
372 OPC contacts evokes rapid and persistent synaptic stabilization.
373
374 Our findings definitively demonstrate that DR axons stop in two distinct ways, forming
375 dystrophic or synaptic contacts. Our EM studies revealed numerous synapses or synapse-like
376 profiles, but no dystrophic endings, in the CNS beyond the borderline. Other investigators also
377 observed synapse-like profiles (termed synaptoids) and postulated the presence of "physiological
378 stop signals" arresting DR axons [54,55]. Together, we suggest that dystrophic endings form
379 exclusively at the border area where OPCs are absent, but collagen fibers are abundant.
380 Considering the much slower axon degeneration and weaker inflammatory responses in the CNS
381 than PNS [56], the extent of intraneural fibrosis is likely high at the border and peripherally along
382 the root [56]. Accordingly, endoneurial fibroblasts proliferate rapidly after peripheral nerve injury
383 [29], and we observed a marked increase of PDGFRα+ fibroblasts peripherally after DR injury.
384 Moreover, our ultrastructural surveys frequently revealed collagen fibers peripherally but rarely
385 at the DREZ. One speculative scenario is, therefore, that regenerating axons exiting basal lamina
386 tubes at the borderline are occasionally obstructed by collagen fibers. Interestingly, extensive
387 fibrosis inhibits OPC migration [57], suggesting that collagen fibers may trap dystrophic endings
388 and also repel OPCs from the PNS.
389
390 Approximately 70% axons did not turn around or stop at the borderline, but invaded CNS
391 territory. This is surprising considering the limited ability of axons to cross astrocyte-Schwann
392 cell interfaces [58,59]. However, axons can use bridges formed by astrocytes to cross the DREZ [60]
393 and spinal cord lesions [61]. Astrocytic processes invade peripherally after DR injury and are
394 frequent within Schwann cell basal lamina tubes [62]. We suggest, therefore, that astrocytic
395 guidance is initiated peripherally and that it enables many axons to cross the borderline.
396
397 When axons crossed the borderline (~5 dpi), proliferating OPCs filled most regions of the DREZ
398 with a dense meshwork of highly ramified processes. Axons that invaded CNS territory would,
399 therefore, almost immediately encounter OPCs and make multiple contacts with OPC processes.
400 If, as we think likely, each axon-OPC contact elicits synaptic induction, then exuberant
401 synaptogenic signals will easily overpower weak growth-promoting stimuli in CNS territory,
402 thereby rapidly arresting axons. OPC-mediated synaptic arrest can, therefore, explain how axons
403 are rapidly immobilized and how arrested axons can be maintained for a remarkably long time

404 without degenerating. Supporting this notion are reports that presynaptic differentiation is rapidly
405 induced within one hour after target contact [63,64]. OPC synapses are formed on multiple discrete
406 sites along unmyelinated axons, where vesicular glutamate release can elicit local Ca signaling
407 on OPCs [37,65]. These neuron-OPC synapses are maintained and transferred to the daughter OPC
408 cells when OPCs divide [66,67].
409
410 OPC-mediated synaptic arrest is also consistent with recent studies implicating synaptic
411 suppression as an important determinant of axon regeneration. DRG neurons downregulate
412 presynaptic proteins essential for synaptic transmission, such as $\alpha_2\delta$ calcium channel subunits, as
413 they regain the ability to grow their axons [68]. Genetic or pharmacological targeting of $\alpha_2\delta$ or
414 another active zone protein, Munc13, promotes regeneration of dorsal column axons after spinal
415 cord injury [68,69]. Intact axon branches maintaining synaptic connections similarly suppress
416 regeneration of injured axon branches [70].
417
418 We suggest that OPCs stop regenerating axons, and that they do so by inducing synaptic
419 differentiation. Silver's group reported the seemingly analogous finding that spinal cord axons
420 dying back after injury stop degenerating by making synapse-like contacts with OPCs [38].
421 NG2/CSPG4 appears to mediate this process, termed synaptic entrapment, because knockout
422 mice globally lacking NG2/CSPG4 show reduced entrapment, lengthened dying-back, and more
423 robust intraspinal regeneration [38]. Notably, however, synapses with clear ultrastructural features
424 were not observed (Jerry Silver, personal communication). OPC-neuron synapses form readily in
425 the absence of NG2/CSPG4 [71]. Additionally, taking into account that the study from the Silver
426 group examined degenerating, not regenerating, axons, we posit that NG2/CSPG4-mediated
427 synaptic entrapment is not identical to OPC-mediated synaptic arrest. It remains to be determined
428 if intraspinal axons stop regenerating by forming synapses with OPCs.
429
430 How OPCs induce presynaptic differentiation remains speculative. OPCs express several
431 synaptogenic molecules, including Nlgn1-3 (Neuroligin1-3), Cadm1a/1b (SynCAM1a/1b), Lrrc4
432 (NGL-3), and Lrrtm 1/2 [72]. Neuroligin and SynCAM are transsynaptic adhesion molecules that
433 trigger presynaptic assembly when expressed in non-neuronal cells [73,74]. Also undetermined is
434 whether the formation of OPC-DR axon synapses requires synaptic transmission or activity.
435 Notably, inhibition of synaptic transmission promotes regeneration of DC axons [68,69], whereas
436 chemogenetic activation of DRG neurons combined with CSPG removal enhances regeneration
437 across the DREZ [75]. Although neuron-neuron synaptogenesis proceeds in the absence of
438 neuronal activity [76,77], neuronal activity levels may have a differential effect on synapse number
439 and maturation in different contexts [78]. It will, therefore, be interesting to determine how activity
440 levels of DRG neurons affect OPC-mediated synaptic arrest.
441
442 To verify the dominant role of OPCs, we sought to determine whether a nerve conditioning
443 lesion would enhance regeneration if OPCs are depleted. However, because a conditioning lesion
444 reduced the efficiency of OPC deletion, we could not obtain conclusive results (data not shown).
445 Attempts to survey the mobility of axons arriving at the DREZ were also unsuccessful, because
446 too many OPCs remained at 5 dpi. It is worth emphasizing, therefore, that we observed enhanced
447 regeneration despite the continued presence of ~30% OPCs at 2 wpi and ~70% OPCs at 4 wpi.
448 Lastly, the ability of OPCs to differentiate into myelinating oligodendrocytes is limited, although
449 surplus numbers are rapidly generated after demyelination [79]. The function of OPC-neuron

synapses also remains enigmatic [36]. Future efforts to determine if OPCs elsewhere in the CNS curtail axon plasticity and/or regeneration, may have significant basic science and clinical implications.

**Limitations of the study**

EM remains the only unbiased method to unequivocally identify synaptic structures and partner cells, but ultrastructurally identifying a cell type is challenging. Our immunoEM identified axon contacts with NG2+ cells exhibiting apparent synaptic features. Although DRG neurons and OPCs were not specifically labeled in the study, it is highly likely that these synaptic contacts are made by regenerating DR axons and OPCs because no other axons are present at the axotomized DREZ and no other NG2+ cells form bona fide synapses. Nevertheless, it is necessary to confirm their identity unambiguously. In addition, although our light microscopic, in vitro, and EM studies all suggest an extensive incidence of axon-OPC synapses, we could not confirm this notion with immunoEM. Advanced technologies, such as genetic labeling, correlative light and electron microscopy and volume imaging will be able to demonstrate definitively the location, incidence, and cellular identity of axon-OPC synapses. Further limitations of the present study include incomplete OPC ablation and concomitant ablation of PDGFRα+ fibroblasts. Future studies that completely and specifically ablate OPCs will confirm and evaluate more fully the effects of OPC ablation on axon regeneration.

**ACKNOWLEDGMENTS**

We thank Drs. Alan Tessler, Tim Himes, George Smith, and Gareth Thomas for critical reading of the manuscript. We thank Dr. Dwight Bergels for guinea pig anti-NG2 antibody, Drs. Dewight Williams and Biao Zuo at the Penn Electron Microscopy Resource Laboratory for technical support for TEM and immunoEM. We sincerely thank Dr. Ahmet Hoke for motivating the study, Drs. Jerry Silver and Theresa Connors for earlier immunoEM efforts, Dr. Michael Lane for pseudorabies virus, Dr. Jian Zhong for WGA-transsynaptic virus and Dr. George Smith for scAAV2-GFP. This work was supported by grants from NIH R01 (NS079631) and Shriners Children's to Y-J Son. H.K. was a recipient of Craig H Neilson postdoctoral fellowship (280274).

**AUTHOR CONTRIBUTIONS**

Conceptualization, Y-J.S.; methodology, S.K., H.H.; investigation, H.K., A.S., J.X., S.H., J.Z., Y-J.S.; writing—original draft, H.K.; writing—review and editing, Y-J.S.; funding acquisition, Y-J.S., H.K.; resources, S.K.,; supervision, Y-J.S.

**DECLARATION OF INTERESTS**

The authors declare no competing interests.

**FIGURE LEGENDS**

**Figure 1. Dystrophic endings form by axons embedded in collagen fibers at the borderline**
**(A, B)** Ultrastructural comparison of synaptic-like profiles (A) and a dystrophic ending (B) formed by DR axons at the DREZ at 2 wpi. The presynaptic axons exhibiting clustered vesicles

496 are small and opposed to unknown postsynaptic cells exhibiting thin postsynaptic density
497 (asterisks), whereas the dystrophic ending is large, disorganized, and embedded in acellular
498 collagen fibers. Scale bar: 500nm
499 **(C)** The incidence and location of dystrophic endings analyzed on transverse sections, at 2 weeks
500 after C5-C8 root crush followed by AAV2-GFP injections to C5 and C7 DRGs. A representative
501 section, with enlarged view, showing a large dystrophic ending (asterisk) formed at the
502 borderline (dotted line). Note that many other axons stopped past the borderline do not display
503 dystrophic endings. Graphs show the incidence of dystrophic endings and their location relative
504 to the borderline (n= >100 axons/mouse, 3 mice; putative synaptic endings, 156.7±19.10;
505 dystrophic endings, 26.33±7.688; locations of dystrophic endings (n=91), 8.308±9.233). Error
506 bars represent SD. Scale bar: 20µm
507 **(D)** High resolution 3D imaging and quantitative analysis of axon endings on wholemounts of
508 CLARITY cleared spinal cords at 2 weeks after L4 and L5 root crush. Transmitted light and
509 fluorescent views of a representative cleared spinal cord, roots, DRG (inset), and GFP+ axons
510 arrested at the DREZ in enlarged (d) or volume rendered images. Representative examples
511 illustrate parental axons that turn around (e.g., 1), form a large dystrophic ending (e.g., 2), or
512 form a small putative synaptic ending (e.g., 3). Relative incidence of different axon endings
513 illustrating that a limited number of parental axons turned around or stopped by forming
514 dystrophic endings. n= >100 axons/mouse, 3 mice. Putative synaptic endings, 116.3±16.33;
515 turned-back axons, 13.67±5.925; dystrophic endings, 19.0±8.185. Error bars represent SD. Scale
516 bars: 200µm (clearing), 50µm (DRG), 50µm (3D, volume), 10µm (enlarged 3D)
517
518 **Figure 2. Two-photon imaging confirms rapid axon immobilization at the DREZ**
519 **(A)** Schematic illustration of the experimental procedure for two-photon imaging of DR axons in
520 live Thy1-YFPM mice after L5 root crush.
521 **(B)** A widefield view of the DREZ area, taken at 5 dpi, showing an axon of interest (arrows) and
522 fluorescent debris of degenerating old axons and a midline vein that served as landmarks
523 (asterisks). Scale bar:100µm
524 **(C, D)** Two-photon imaging of representative axon tips with either slender (C) or small roundish
525 shape (D), taken every 30 min on 5 dpi. Arrows denote immobile axon tips and asterisks denote
526 landmarks. Scale bar: 50µm (C, D), 20µm (D, insets)
527
528 **Figure 3. Relative positions of non-neuronal cells and arrested axons at the DREZ**
529 **(A, B)** Transverse sections of a spinal cord 2 weeks after cervical root crush followed by
530 intraganglionic injection of AAV2-GFP.
531 **(A)** A DREZ area illustrating spatial relationships of arrested GFP+ axons (Green) with GFAP-
532 labeled astrocytes (Blue) and p75-labeled Schwann cell processes (B/W). Many axons extend
533 across the borderline (dotted line) by growing through astrocytes without association with
534 leading Schwann cell processes. Scale bar: 50µm
535 **(B)** A DREZ area illustrating spatial relationships of arrested axons (refer to A) with MOG-
536 labeled oligodendrocytes (Blue), SC2E-labeled myelinating Schwann cells (Magenta), and ED1-
537 labeled macrophages (B/W). Macrophages are sparse at the DREZ. Scale bar: 50µm
538 **(C)** Diagram summarizing insignificant spatial relationships of arrested axons with
539 oligodendrocytes, astrocytes, Schwann cells, and macrophages at axotomized DREZ.
540 **(D)** A DREZ area of uninjured DRs illustrating that NG2-labeled OPCs (B/W) are absent at and
541 immediately near the borderline (dotted line), denoted by astrocytes (Blue) and oligodendrocytes

542 (Magenta), but abundant deeper at the DREZ (>50μm from the borderline). Arrow denotes
543 NG2+ pericytes associated with a blood vessel. Scale bar: 50μm
544 **(E)** Diagram illustrating the distance and position of OPC processes relative to the borderline
545 (dotted line) at intact DREZ with no axon injury.
546 See also **Figure S1 and S2**
547
548 **Figure 4. Stopped axons without dystrophic endings display extensive contacts with OPC**
549 **processes**
550 **(A)** Wholemount views of the DREZ area in low and high magnifications at 2 wpi, showing
551 GFP+ axons (Green), NG2-labeled OPCs (Magenta), and p75-labeled Schwann cells (Blue).
552 Arrows indicate examples of direct contacts between OPC processes and arrested axons. NG2
553 staining in the PNS (asterisks) is intense after DR injury but does not preclude identification of
554 OPC processes. Scale bar: 100μm
555 **(B)** Transverse sections in low and high (b) magnifications showing GFP+ axons (Green) and
556 NG2-labeled OPCs (Magenta) at 2 wpi. Arrowheads indicate an example of many axons that
557 stopped past the borderline (dotted line) in association with OPC processes. Arrows indicate a
558 dystrophic ending formed at the borderline that, in contrast, lacks contacts with OPC processes.
559 Scale bar: 50μm
560
561 **Figure 5. DR axons arrested at the DREZ form synapses with OPC processes**
562 **(A)** Wholemount views of the DREZ area at 2 wpi in low and high magnifications (a), showing
563 GFP-labeled axons (Green), SV2-labeled synaptic vesicles (B/W), and NG2-labeled OPCs
564 (Magenta). Boxed area shows several axons with small swellings on axon tips and shafts
565 intensely labeled for SV2 and tightly associated with OPC processes. Asterisks indicate same
566 positions. Scale bar: 100μm (A), 50μm (a)
567 **(B)** Volume rendered image (b) of a boxed area in B, illustrating direct contacts of axon
568 swellings (Green) with OPC processes (Magenta). Scale bar: 5μm
569 **(C)** Diagram showing procedures to prepare a longitudinal vibratome slice of dorsal spinal cord
570 with attached DR at 2 wpi.
571 **(D)** An electron micrograph of the PNS area showing gold particles (arrows) targeted to NG2
572 selectively labeling Schwann cells (SC). Scale bar: 500 nm
573 **(E)** An area of the DREZ showing that OPC processes denoted by gold particles (arrows) form
574 synaptic contacts with axons. Magnified view of boxed area (e) illustrates synaptic profiles
575 (asterisks) with presynaptic clustering of synaptic vesicles and postsynaptic density. Scale bar:
576 100 nm
577 **(F)** An electron micrograph illustrating varicosity-like synaptic profile formed by DR axon
578 encircled by OPC processes identified by gold particles (arrows). Scale bar: 100 nm
579 See also **Figure S3**
580
581 **Figure 6. Genetic OPC ablation, although incomplete, markedly enhances regeneration**
582 **across the DREZ**
583 **(A)** Diagram illustrating experimental procedures to evaluate the effects of genetic OPC ablation
584 at 2 weeks after C5-C8 root crush followed by AAV2-GFP injections to C5 and C7 DRGs.
585 **(B)** Western blotting showing markedly reduced markers of OPCs, NG2, and PDGFRα, in
586 PDGFRα-DTA mice.

587 **(C)** Quantitative comparisons of OPC density measured by mean fluorescence intensity of NG2
588 staining in the spinal cord, illustrating ~70% ablation of OPCs in PDGFRα-DTA mice used for
589 the analysis. Cntl, 100.0±8.992; DTA, 33.07±5.725. Error bars represent SD. Unpaired t test
590 (n=5 control, 6 DTA mice). ****$p \leq 0.00001$
591 **(D)** Transverse sections of a control and a PDGFRα-DTA mouse with ~80% OPC ablation at 2
592 wpi showing GFAP-labeled astrocytes (Blue), NG2-labeled OPCs (Magenta), and GFP+ axons
593 (Green). Enlarged views of boxed area (d1, 1, 2) illustrate that more axons cross the border and
594 DREZ in the PDGFRα-DTA mouse. Blue lines approximate ~100μm wide region of the DREZ.
595 Dotted lines denote borderline identified by GFAP staining. Insets are magnified views of the
596 DREZ, illustrating residual and/or repopulating OPCs in PDGFRα-DTA mice. An arrow denotes
597 axons extending unusually deeply into the dorsal funiculus. Scale bar: 100μm, 50μm (insets)
598 **(E)** Quantification of GFP+ axons at ~100μm proximal to the borderline in the PNS. Cntl,
599 13.86±1.075; DTA, 15.76±1.052. Error bars represent SEM (n = 4 mice/group). Unpaired
600 Student's t-test. ns, $p > 0.05$
601 **(F)** Quantitative comparisons of control and PDGFRα-DTA mice illustrating that OPC ablation
602 triples the number of axons extending past the DREZ. Cntl: 0μm, 1.00±0; 100μm,
603 0.0765±0.02744; 200μm, 0.02128±0.01181; 300μm, 0.00±0.00. DTA: 0μm, 1.00±0.00; 100μm,
604 0.3167±0.0485; 200μm, 0.08238±0.04858; 300μm, 0.01723±0.01723; 400μm,
605 0.001375±0.001375. Error bars represent SEM (n=4 mice/group). Two-way repeated-measures
606 ANOVA with Tukey's multiple comparisons test. 100μm, ****$p \leq 0.00001$; 200μm, ns, $p >$
607 $0.05$; 300μm
608 See also **Figure S4, S5, S6**
609
610 **Figure 7. Axons continue regenerating intraspinally through areas lacking OPCs**
611 **(A)** Diagram illustrating experimental procedures to evaluate the effects of genetic OPC ablation
612 at 4 weeks after C5-C8 root crush followed by AAV2-GFP injections into C5 and C7 DRGs.
613 **(B)** Quantitative comparison of OPC density, measured by mean fluorescence intensity of NG2
614 staining in the spinal cord, illustrating ~30% ablation of OPCs in PDGFRα-DTA mice used for
615 the analysis. Cntl, 100.0±23.35; DTA 72.31±11.4. Error bars represent SD. Unpaired t test (n=4
616 control, 5 DTA mice). ns, $p > 0.05$
617 **(C)** Quantification of GFP+ axons at ~100μm proximal to the borderline, illustrating
618 insignificant difference between control and PDGFRα-DTA mice. Cntl, 13.98±2.281; DTA
619 15.53±2.063. Error bars represent SEM (n = 4 mice/group). Unpaired Student's t-test. ns, $p >$
620 $0.05$
621 **(D)** Transverse sections from a control and a PDGFRα-DTA mouse, illustrating massive
622 repopulation of OPCs and GFP+ axons that regenerate remarkably deeply into the dorsal horn
623 (arrows). There are noticeably fewer OPC processes where more axons (arrowheads) regrow
624 within the spinal cord (area 1) than where fewer axons (arrows) regenerate (area 2). Enlarged
625 view of boxed area (d) illustrates regenerated GFP+ axons in association with repopulated OPC
626 meshwork. Scale bar: 100μm
627 **(E)** Quantitative comparison of control and PDGFRα-DTA mice illustrating that ~20% axons
628 continue to regenerate past the DREZ in DTA mice during the additional two weeks. Error bars
629 represent SEM (n=4 mice/group). Two-way ANOVA with Sidak's multiple comparisons test.
630 100μm; ns, $p > 0.05$ (DTA 4 wpi vs. DTA 2 wpi); ****$p \leq 0.00001$ (DTA 4 wpi vs. control 4

wpi), 200μm; ****$p \leq 0.00001$ (DTA 4 wpi vs. control 4 wpi), *$p \leq 0.01$ (DTA 4 wpi vs. DTA 2 wpi), 300μm; ns, $p > 0.05$ (DTA 4 wpi vs. control 4 wpi, DTA 2 wpi).
**(F)** Schematic illustration of the proposed model.
See also **Figure S7**.

## SUPPLEMENT FIGURE LEGENDS

**Figure S1. Macrophages, pericytes, fibroblast-like cells, and blood vessels are sparse at intact and axotomized DREZ**

**(A)** Transverse sections of a spinal cord at 2 wpi, showing low and high magnification views of DREZ area. Asterisks denote numerous macrophages (Magenta) enriched peripherally along the root. Macrophages are sparse at the DREZ and NG2+ (Green). Yellow dotted line denotes borderline identified by peripherally enriched nuclei. White dotted line denotes grey matter. Scale bar: 100μm

**(B)** Transverse sections of a spinal cord at 2 wpi, showing low and high magnification views of the DREZ area. Pericytes and VLMCs, labeled by PDGFRβ (Magenta), are sparse at the DREZ and appear to be perivascular as indicated by those within the spinal cord. Arrows denote PDGFRβ+/NG2-/PDGFRα+ meningeal fibroblasts associated with the nerve root. NG2 and PDGFRα staining overlaps closely at the DREZ. Because few if any other types of NG2+/PDGFRα+ cells (i.e., VLMCs) are present at the DREZ, almost all NG2+ cells at the DREZ are OPCs and their processes. Scale bar: 100μm

**(C)** Transverse sections of a spinal cord at 2 wpi, showing high magnification views of grey matter. All pericytes and VLMCs, labeled by PDGFRβ (White arrowheads), remain associated with blood vessels (B/W) after DR injury. Some PDGFRβ labeling is not co-localized with PDGFRα staining (Magenta arrowheads), consistent with the notion that VLMCs, but not pericytes, express PDGFRα. Scale bar: 100μm

**(D)** Low magnification views of transverse sections of a spinal cord showing an intact (right) and severely avulsed (left) root. Glial/fibrotic scar was intentionally elicited by severely avulsing C5-C6 roots to damage dorsal spinal cord. The scar is filled with numerous PDGFRβ+ cells. In contrast, PDGFRβ+ cells are sparse at the DREZ (asterisks) and spinal cord with an intact root or after root crush (**B**). Note also that blood vessels (Green) are sparse at the DREZ. Scale bar: 100μm

**Figure S2. OPCs proliferate, migrate, and form a dense meshwork of processes after DR injury**

**(A, B)** Wholemount views of intact (A) and axotomized (B) DREZ area showing subsets of YFP+ axons (Green) and the distribution of NG2-labeled OPCs and their processes (Magenta). Dotted line approximates the borderline denoted by GFAP-labeled astrocytes (B/W, Blue). Enlarged images (a, b) show area near the borderline (asterisks) and deeper in CNS territory. Scale bar: 100μm

**(C)** Transverse sections of intact or axotomized DREZ at 5 dpi and 2 wpi, co-labeled for NG2 (Magenta) and GFAP (B/W, Blue), illustrating temporal development of a dense meshwork of OPC processes populating the DREZ after DR injury. Asterisk denotes NG2-labeled blood vessels. Scale bar: 50μm

676 **(D)** Quantification of OPC proliferation by counting nuclei co-labeled by Olig2, a marker of
677 OPCs and oligodendrocytes, and Ki67, a marker of cell proliferation. N= >3 sections/each
678 mouse, 5 mice/each time point. Ki67+Olig2+: intact, 5.405±3.310; 3 dpi, 29.23±4.260; 1 wpi,
679 8.359±1.945; 2 wpi. 4.047±1.845. Olig2+: intact, 9.967±1.327; 3 dpi, 13.09±1.082; 1 wpi,
680 18.68±1.859; 2 wpi 14.87±2.065. Error bars represent SEM. p values are calculated by one-way
681 repeated measures ANOVA with Tukey's post hoc test. ns, $p > 0.05$; *$p \leq 0.01$, **$p \leq 0.001$,
682 ***$p \leq 0.0001$.
683
684 **Figure S3. OPCs form functional synapses with co-cultured DRG neurons**
685 **(A)** >95% pure OPCs, cultured from spinal cords of p16-18 mice, immunolabeled at 3 div for
686 DAPI, Olig2, NG2 and PDGFRα. Enlarged view (a) of boxed area illustrates OPCs with bushy
687 processes resembling OPCs *in vivo*. Scale bar: 20μm
688 **(B)** Purified OPCs and DRG neurons co-cultured for 5 days, showing DAPI, NG2-labeled OPCs,
689 Tuj1-labeled axons, and SV2-labeled synaptic vesicles. Magnified view (b) of boxed area
690 illustrates microtubule-deficient but SV2-enriched axonal swellings (arrows) formed on OPCs.
691 Scale bar: 50μm
692 **(C)** Representative calcium imaging recordings of OPC-DRG neurons co-cultured for 5 days,
693 illustrating temporal calcium responses of a neuron (Black arrows) and two adjacent OPCs
694 (Green and Magenta arrows), following capsaicin stimulation of neurons without (C1) or with
695 antagonists of AMPA/kainate and NMDA receptors (C2), CNQX and AP5. Following washout
696 of antagonists (C3), capsaicin stimulation of the same neuron again elicits calcium responses in
697 the same OPCs. Graph shows comparisons of capsaicin-elicited calcium responses in DRG
698 neurons and OPCs. n = 7-18. Neurons, 0.76±0.05; OPCs, 0.22±0.06; OPCs, 0.05± 0.04. Error
699 bars represent SEM. p values are calculated by one-way repeated measures ANOVA with
700 Tukey's post hoc test. ***$p \leq 0.001$, ****$p \leq 0.0001$. Scale bar: 30μm
701
702 **Figure S4**. **Pericytes and ablation of PGFRα+ cells in PDGFRα-DTA mice**
703 **(A)** Representative high magnification views of the DREZ area in a control and two PDGFRα-
704 DTA mice, co-labeled for PDGFRα, NG2, and PDGFRβ. A PDGFRα-DTA mouse with ~40%
705 OPC ablation at 2 wpi shows PDGFRα staining closely overlapped with NG2 staining,
706 illustrating ablation of PDGFRα+ cells. Bottom panels show the DREZ area of an uninjured
707 PDGFRα-DTA mouse with ~80% OPC ablation, illustrating unaffected pericytes.
708 NG2+/PDGFRβ+ cells with perivascular morphology (i.e., pericytes; arrows) remain intact,
709 despite almost complete ablation of PDGFRα+ cells in the DREZ area of the DTA mouse. Scale
710 bar: 50μm
711 **(B)** Quantitative comparisons of control and PDGFRβ-DTA mice, illustrating a reduction of
712 PDGFRβ immunoreactivity in the spinal cord of DTA mice. Quantification of the DREZ area is
713 not provided due to paucity of PDGFRβ+ cells at the DREZ in both control and DTA mice. Cntl,
714 28.74±3.344; DTA, 17.69±0.6118**.** Unpaired Student t-test (n=3 control, 3 DTA mice). Error
715 bars represent SEM. *$p \leq 0.01$.
716 **(C)** High magnification views of dorsal roots of a PDGFRα-tdTomato mouse, showing that
717 PDGFRα+ cells are sparse in an intact dorsal root but abundant in a crushed root at 2 wpi.
718 PDGFRα+ cells are not labeled by Sox10 (arrows), indicating that they are not Schwann cells.
719 Scale bar: 50μm

720 **(D)** High magnification views of intact and crushed dorsal roots of a PDGFRα-tdTomato mouse,
721 showing that PDGFRα+ cells are co-labeled by a fibroblast marker, vimentin (arrows). Scale
722 bar: 50μm
723 **(E)** Quantitative comparisons of control and PDGFRα-DTA mice, illustrating insignificant
724 difference in PDGFRα immunoreactivity in the dorsal root. Cntl, 28.04±1.406; DTA.
725 21.83±2.197. Unpaired Student t-test (n=4 mice/group). Error bars represent SEM. ns, $p > 0.05$
726
727 **Figure S5**. **Microglia, macrophages and astrocytes in PDGFRα-DTA mice**
728 **(A)** Transverse sections of a control and a PDGFRα-DTA mouse at 2 wpi, showing DAPI and
729 Iba1-labeled microglia, and illustrating no noticeable differences in morphology or density of
730 microglia in the spinal cord, DREZ, or DR of control and DTA mice. Scale bar: 100μm
731 **(B)** Transverse sections from a control and PDGFRα-DTA mouse at 2 wpi, showing DAPI and
732 ED1-labeled macrophages, and illustrating no noticeable differences in the distribution or density
733 of macrophages in the spinal cord, DREZ, or DR of control and DTA mice. Scale bar: 100μm
734 **(C)** Transverse sections of control and PDGFRα-DTA mice at 2 wpi, co-labeled for NG2 and
735 GFAP, illustrating no noticeable differences in the density or distribution of astrocytes at the
736 DREZ or within the spinal cord between control and DTA mice. Scale bar: 50μm
737 **(D)** Quantitative comparisons of control and PDGFRα-DTA mice illustrating insignificant
738 difference in the number of Iba1+ microglia in the spinal cord. Cntl, 207.8±21.20; DTA,
739 202.1±12.70. Unpaired Student's t-test (n=3 mice/group). Error bars represent SEM. ns, $p > 0.05$
740 **(E, F)** Quantitative comparisons of control and PDGFRα-DTA mice, illustrating insignificant
741 difference in the number of ED1+ macrophages in the spinal cord (E) or dorsal root (F). (E) Cntl,
742 14.50±1.258; DTA, 13.00±0.5774. (F) Cntl, 43.00±2.179; DTA, 52.94±7.330. Unpaired
743 Student's t-test (n=3 mice/group). Error bars represent SEM. ns, $p > 0.05$
744 **(G)** Quantitative comparisons of control and PDGFRα-DTA mice, illustrating insignificant
745 difference in GFAP immunoreactivity in the spinal cord. Cntl, 90.10±4.363; DTA, 78.95±4.127.
746 Unpaired Student's t-test (n=3 mice/group). Error bars represent SEM. ns, $p > 0.05$
747
748 **Figure S6**. **NG2/CSPG4, Schwann cells and CSPGs in PDGFRα-DTA mice**
749 **(A)** Transverse sections of a control and a PDGFRα-DTA mouse with ~80% OPCs ablated at 2
750 wpi, co-labeled for NG2 and GFAP, illustrating a marked reduction in OPCs and their processes
751 in PDGFRα-DTA mouse. NG2 staining is slightly reduced peripherally along the DR of the
752 PDGFRα-DTA mouse, as compared to control mouse. Scale bar: 100μm
753 **(B)** Transverse sections of control and PDGFRα-DTA mice at 2 wpi, illustrating that p75
754 immunoreactivity in dorsal root of DTA mouse is comparable to that of control mouse. Scale
755 bar: 500μm
756 **(C)** Transverse sections of control and PDGFRα-DTA mice at 2 wpi, illustrating no noticeable
757 difference in the number of Sox10-labeled Schwann cells present in the dorsal root. Scale bar:
758 100μm
759 **(D)** Transverse sections of a control and a PDGFRα-DTA mouse, co-labeled for NG2 and for
760 CS56 at 2 wpi, showing reduced NG2 but abundant CSPGs associated with the DREZ area of
761 DTA mice. Scale bar: 100μm
762 **(E)** Quantitative comparisons of control and PDGFRα-DTA mice, illustrating a slight reduction
763 of NG2 immunoreactivity in dorsal roots of DTA mice. Cntl, 18.81±1.419; DTA, 13.81±1.173.
764 Unpaired Student's-t test (n=5 control, 6 DTA mice). Error bars represent SEM. $*p \leq 0.01$

765 **(F)** Quantitative comparison of control and PDGFRα-DTA mice, illustrating insignificant
766 difference in p75 immunoreactivity in the dorsal root. Cntl, 153.7±11.83; DTA, 117.5±18.55.
767 Unpaired Student's t-test (n=3 mice/group). Error bars represent SEM. ns, $p > 0.05$
768 **(G)** Quantitative comparison of control and PDGFRα-DTA mice, illustrating insignificant
769 difference in the number of Schwann cells in the dorsal root. Cntl, 195.0±17.03; DTA
770 182.1±14.19. Unpaired Student's t-test (n= 4 control, 5 DTA mice). Error bars represent SEM.
771 ns, $p > 0.05$
772 **(H)** Quantitative comparisons of control and PDGFRα-DTA mice, illustrating insignificant
773 difference in CS56 immunoreactivity measured in the dorsolateral funiculus including the
774 DREZ. Cntl, 99.58.0±4.926; DTA 92.46±5.748. Unpaired Student's t-test (n=3 control, 3 DTA
775 mice). Error bars represent SEM. ns, $p > 0.05$
776
777 **Figure S7**. **Axons regenerate deeper into the dorsal funiculus in PDGFRα-DTA mice at 4**
778 **wpi**
779 **(A, B)** Two sets of transverse sections of PDGFRα-DTA mice at 4 wpi, co-labeled for GFAP
780 and NG2, illustrating more numerous GFP+ axons (Green) that regenerated deeper into the
781 dorsal funiculus than at 2 wpi (refer to Figure 7D). These axons terminate where OPCs are
782 locally repopulated, in association with OPC processes (Magenta). Enlarged views of boxed area
783 also indicate sparse distribution of OPCs where these axons regenerate. Arrows show axons
784 reaching more deeply into the dorsal horn. Scale bar: 50μm
785
786
787 **STAR METHODS**
788
789 **Key resources table**

| REAGENT or RESOURCE | SOURCE | IDENTIFIER |
|---|---|---|
| Antibodies | | |
| Rabbit polyclonal anti-GFAP | Dakocytomation | Cat# N1506; RRID: AB_10013482 |
| mouse monoclonal anti-GFAP | Sigma-Aldrich | Cat# G3893; RRID: AB_477010 |
| Goat polyclonal anti-MOG | R&D Systems | Cat# AF2439; RRID: AB_2145537 |
| Mouse monoclonal anti-SC2E | Cosmo Bio Co | Cat# CAC-GU01-M01AS-A; RRID: AB_1962608 |
| Goat polyclonal anti-p75NGFR | Neuromics | Cat# GT15057; RRID: AB_1611758 |
| Rat polyclonal anti-ED1 | AbD serotec | Cat# MCA1957; RRID: AB_322219 |
| Rabbit polyclonal anti-CGRP | Peninsula Lab | Cat# T-4032; RRID: AB_2307330 |

| | | |
|---|---|---|
| Rabbit polyclonal anti-NF200 | Sigma-Aldrich | Cat# N4142; RRID: AB_477272 |
| Mouse monoclonal anti-SV2 | Developmental Studies Hybridoma Bank | Cat# SV2; RRID: AB_2315387 |
| Guinea pig polyclonal anti-NG2 | Dr. Dwight Bergles | N/A |
| Rat polyclonal anti-PDGFRα | BD Biosciences | Cat# 558774; RRID: AB_397117 |
| Rabbit-monoclonal anti-PDGFRα | abcam | *Cat# ab203491; RRID: AB_2892065* |
| Mouse monoclonal anti-PDGFRβ | abcam | *Cat# ab69506; RRID:AB_1269704* |
| Mouse monoclonal anti-APC-CC1 | Millipore | Cat# OP80; RRID: AB_213434 |
| Goat polyclonal anti-CD31/PECAM1 | R&D Systems | Cat# AF3628; RRID:AB_2161028 |
| Goat polyclonal anti-Sox10 | R&D Systems | Cat# AF2864; RRID:AB_442208 |
| Rabbit monoclonal anti-Vimentin | abcam | Cat# ab92547; RRID:AB_10562134 |
| Mouse monoclonal anti-CS56 | Sigma-Aldrich | Cat# C8035; RRID:AB_476879 |
| Rabbit polyclonal anti-GFP | abcam | Cat# ab290; RRID: AB_303395 |
| Rabbit polyclonal anti-olig2 | Millipore | Cat# AB9610; RRID: AB_570666 |
| Rabbit polyclonal anti-Ki67 | Millipore | Cat# AB9260; RRID: AB_2142366 |
| Rabbit polyclonal anti-NG2 IgG | Millipore | Cat# AB5320; RRID: AB_91789 |
| Mouse polyclonal anti-β-actin | Sigma-Aldrich | Cat# A5441; RRID: AB_476744 |

| | | |
|---|---|---|
| Goat anti-mouse IgG (H+L), FITC | Invitrogen | Cat# A10530; RRID: AB_2534035 |
| Goat anti-mouse IgG (H+L), Alexa Fluor 568 | Invitrogen | Cat# A21124; RRID: AB_141611 |
| Goat anti-rabbit IgG (H+L), FITC | Invitrogen | Cat# A11034; RRID: AB_2576217 |
| Goat anti-rabbit IgG (H+L), Alexa Fluor 568 | Invitrogen | Cat# A11011; RRID: AB_143157 |
| Goat anti-rabbit IgG (H+L), Alexa Fluor 647 | Invitrogen | Cat# A21244; RRID: AB_141663 |
| Donkey anti-rabbit IgG (H+L), Alexa Fluor 546 | Invitrogen | Cat# A10040; RRID: AB_2534016 |
| Donkey anti-rabbit IgG (H+L), Alexa Fluor 647 | Invitrogen | Cat# A31573; RRID: AB_2536183 |
| Donkey anti-goat IgG (H+L), Alexa Fluor 488 | Invitrogen | Cat# A11055; RRID: AB_142672 |
| Donkey anti-rat IgG (H+L), TRITC | Jackson ImmunoResearch Laboratories | Cat# 712-025-150; RRID: AB_2340635 |
| Donkey anti-guinea pig IgG (H+L), Cy3 | Jackson ImmunoResearch Laboratories | Cat# 706-166-148; RRID: AB_23404061 |
| Donkey anti-guinea pig IgG (H+L), Dye 647 | Jackson ImmunoResearch Laboratories | Cat# 706-606-148; RRID: AB_2340477 |
| Goat anti-rabbit IgG (H+L), HRP | Santa Cruz | Cat# SC2030; RRID: AB_631747 |
| Goat anti-mouse IgG (H+L), HRP | Jackson ImmunoResearch Laboratories | Cat# 115-035-174; RRID: AB_2338512 |
| Goat anti-rat IgG (H+L), HRP | Jackson ImmunoResearch Laboratories | Cat# 112-035-003; RRID: AB_2338128 |

| | | |
|---|---|---|
| Goat anti-guinea pig IgG (H+L), 10nm gold particles | EMS | Cat# 25329 |
| Bacterial and virus strains | | |
| scAAV2-eGFP | Dr. George M Smith | N/A |
| Chemicals, peptides, and recombinant proteins | | |
| Ketamine | Covetrus | Cat# 11695-0703-1 |
| Xylazine | Akom, Inc. | Cat# 59399-110-20 |
| Buprenorphine | Par pharmaceuticals | Cat# 42023-0179-05 |
| Euthasol | Virbac | Cat# 051311-050-01 |
| paraformaldehyde | EMS | Cat# 157-8 |
| glutaraldehyde | EMS | Cat# 16320 |
| 0.1M phosphate buffer | EMS | Cat# 19340-72 |
| 4-hydoxytamoxifen | Sigma-Aldrich | Cat# H6278 |
| DiI | invitrogen | Cat# N22880 |
| Kwik-Sil | World Precision Instruments, Inc. | Kwik-sil |
| Epredia™ M-1 Embedding Matrix | Thermo Scientific | Cat# 1310 |
| Vectershield | Vector Laboratories | Cat# H-1000 |
| Glycine powder | Sigma-Aldrich | Cat# 50046 |
| Bovine Serum Albumin | Sigma-Aldrich | Cat# A3059 |
| Triton X-100 | Sigma-Aldrich | Cat# T8787 |
| Osmium tetoxide | EMS | Cat# 19150 |
| Araldite 6005 | EMS | Cat# 10920 |
| Uranly acetate | EMS | Cat# 22400 |

| | | |
|---|---|---|
| Sodium Citrate | EMS | Cat# 21140 |
| Toluidine Blue O | EMS | Cat# 22050 |
| Borax | EMS | Cat# 21130 |
| photo-initiator 2,20-Azobis[2-(2-imidazolin-2-yl) propane] dihydrochloride | Wako Chemicals USA | Cat# VA-044 |
| acrylamide | Bio-Rad | Cat# 161-0140 |
| Bis-acrylamide | Bio-Rad | Cat# 161-0142 |
| Boric acid | Sigma-Aldrich | Cat# B7901 |
| SDS | Sigma-Aldrich | Cat# L337 |
| FocusClear | CelExplorer | Cat# FC-1010 |
| ECL Plus | GE Healthcare | Cat# RPN2236 |
| Anti-BSC1 Griffonia Simplificonia (BSL1) | Vector Laboratories | Cat# L1100; RRID: AB_2336491 |
| DMEM | Gibco | Cat# 11960-044 |
| B27 supplement | Gibco | Cat# 17504-044 |
| sodium pyruvate | Gibco | Cat# 11360-070 |
| insulin | Sigma-Aldrich | Cat# I6634 |
| Apo-transferrin | Sigma-Aldrich | Cat# T1147 |
| bovine serum albumin | Sigma-Aldrich | Cat# A4161 |
| progesterone | Sigma-Aldrich | Cat# P8783 |
| putrescine | Sigma-Aldrich | Cat# 5780 |
| sodium selenite | Sigma-Aldrich | Cat# S5261 |
| N-acetyl-L-cysteube (NAC) | Sigma-Aldrich | Cat# C7477 |
| PDGF | Sigma-Aldrich | Cat# SRP3228 |
| bFGF | Sigma-Aldrich | Cat# SRP4038 |

| | | |
|---|---|---|
| Hank's balanced salt solution (HBSS) | Sigma-Aldrich | Cat# H6648 |
| dispase II | Roche Applied Sciences | Cat# 04942078001 |
| HEPES-buffered saline | Sigma-Aldrich | Cat# 51558 |
| Percoll gradient | GE Healthcare | Cat# 17-0891-01 |
| fura-2AM | Thermo Scientific | Cat# J62728.MCR |
| Experimental models: Organisms/strains | | |
| Mouse: Thy1-YHFM | | |
| Mouse: Thy1-YHFH | | |
| Mouse: PDGFRα-creER$^{TM}$ | Jackson Laboratory | RRID: IMSR_JAX:018280 |
| Mouse: Rosa-DTA | Jackson Laboratory | RRID: IMSR_JAX:009669 |
| Mouse: Pngfα-CreER$^{T2}$ | Jackson Laboratory | RRID:IMSR_JAX:032770 |
| Mouse: Ai14 | Jackson Laboratory | RRID:IMSR_JAX:007914 |
| Software and algorithms | | |
| MetaFluor Fluorescence Ratio Imaging software | Molecular devices | RRID: SCR_014294 |
| AxioVision Imaging System | Zeiss | RRID: SCR_002677 |
| Leica LAS AF software | Leica | RRID: SCR_013673 |
| Imaris | Bitplane | RRID: SCR_007370 |
| Photoshop | Adobe | RRID: SCR_014199 |
| Prism 9 | GraphPad | RRID: SCR_002798 |
| ImageJ | NIH | RRID: SCR_003070 |
| Fiji | NIH | RRID: SCR_002285 |
| Other | | |
| Superfrost Plus microscope slides | Fisher Scientific | Cat# 22-230-892 |

| | | |
|---|---|---|
| Leica TCS SP5 II multi-photon confocal microscope | Leica Microsystems | N/A |
| Leica SP8 confocal microscope | Leica Microsystems | N/A |
| epifluorescence M2 microscopy | Zeiss | N/A |
| Leica Ultracet R microtome | Leica Microsystems | N/A |
| Leica cryostat | Leica Microsystems | Cat# CM3050S |
| Diamond knife (Ultra 45º, 4mm) | Diatom | N/A |
| Biobrane | UDL Laboratories, Inc. | Cat# 8459-0095-25 |
| Gore Preclude MVP Dura Substitute | Gore and Associates | Cat# 1MVP401 |
| 6-0 suture | Myco medical | Cat# SK681-SI |

## Resource availability

### Lead contact

Further information and requests for resources and reagents should be directed to and will be fulfilled by the lead contact, Young-Jin Son (**yson@temple.edu**).

### Materials availability

All reagents generated in this study are available from the lead contact without restriction.

### Data and code availability

- All data reported in this paper will be shared by the lead contact upon request.
- This paper does not report the original code.
- Any additional information required to realize the data reported in this paper is available from the lead contact upon request.

## Experimental model and subject details

## Animals

All animal care and procedures were conducted in accordance with the National Institute of Health guidelines and with approval from the Institutional Animal Care and Use Committee at Lewis Katz School of Medicine at Temple University. For *in vivo* imaging or CLARITY tissue clearing, C57BL/6J or the transgenic strains, *Tg(Thy1-EGFP)MJrs/J* (Thy1-GFP-M; JAX 007788) or *B6.Cg-Tg(Thy1-YFP)HJrs* (Thy1-YFP-H; JAX 003782) were purchased from Jackson Laboratory. For OPC ablation, *B6N.Cg-Tg(Pdgfra-cre/ERT)467Dbe/J* (PDGFRα-creER$^{TM}$; JAX 018280) and *B6.129P2-Gt(ROSA) 26Sor$^{tm1(DTA)Lky/J}$* (Rosa26-DTa; JAX 009669) purchased from Jackson Laboratory were crossed to generate *PDGFRα-creER$^{TM}$; Rosa26-DTa* mice. *B6.129S-Pdgfrα$^{tm1.1(cre/ERT2)Blh}$*/J (PDGFRα-CreER$^{T2}$; JAX:032770) and *B6.Cg-Gt(ROSA)26Sor$^{tm14(CAG-tdTomato)Hze}$/J* (Ai14; JAX:007914) from Jackson Laboratory were crossed to generate PDGFRα-tdTomato reporter mice. Adult mice of either sex, 2-3 months old, were used for all experiments. Age matched *PDGFRα-creER$^{TM}$* or *Rosa26-DTa* mice were used as the control.

## Method details

### Dorsal root crush

For unilateral cervical (C5-C8) or lumbar (L4 and L5) root crush, mice were anesthetized with an intraperitoneal injection of xylazine (8 mg/kg) and ketamine (120 mg/kg). Following a 2- to 3-cm-long incision in the skin of the back, the spinal musculature was reflected and the C5-C8 or L3–S1 spinal cord segments exposed by hemilaminectomies. A small incision was made in the dura overlying each targeted DR. A fine forceps (Dumont #5; Fine Science Tools, Foster City, CA) was introduced subdurally and each DR was crushed for 10 s. To avoid scar formation and possible compression, we applied a piece of thin silastic membrane (Biobrane, Bertek Pharmaceuticals, Sugarland, TX) over the hemilaminectomy site and covered it with a layer of thicker artificial dura (Gore Preclude MVP Dura Substitute, W.L. Gore and Associates, Flagstaff, AZ). The overlying musculature was closed with 6-0 sutures, and the skin closed with wound clips. All animals received subcutaneous injections of saline (0.9% w/v NaCl) and buprenorphine (0.05 mg/kg) for postoperative pain management.

### Intraganglionic injection of AAV2-GFP

Recombinant adeno-associated virus 2 carrying eGFP (AAV2-GFP) with CMV-enhanced chicken β-actin (CAG) promoter was purchased from Vector Biolabs (Malvern, PA; stock #7072) or generated as previously described (Liu et al., 2014). AAV2-GFP was microinjected into a DRG using a micropipette pulled to a diameter of 0.05 mm and a nanoinjector (B203XVY Nanoliter 2000; World Precision Instruments, Sarasota, FL). For each injection, the micropipette was introduced 0.5 mm into the DRG and a total volume of AAV (1 µl/DRG) containing >1 X $10^{13}$ GC/ml injected over a 10 min period. The glass needle was left in place for 5 min after each injection.

### 4-HT administration

For OPC ablation, 4-hydroxytamoxifen (4-HT; Sigma # H7904, St. Louis, MO) was injected into 2-3 months old *PDGFRα-CreERTM;ROSA26-iDTa* mice. A 20 mg/ml stock of 4-HT in 100% ethanol was prepared by sonication, and a 1 mg aliquot mixed 1:5 with sunflower oil. After evaporation of the ethanol by speedvac, 1 mg of 4-HT was injected intraperitoneally once daily for 5 consecutive days beginning 2 dpi.

851
852 **CLARITY tissue clearing**
853 Longitudinal slices of the dorsal spinal cord (<1mm thick) were optically cleared using the
854 CLARITY protocol modified for passive clearing (Tomer et al., 2014). Adult mice that received
855 unilateral L4 and L5 root crush, followed by AAV2-GFP intraganglionic injections, were
856 perfused at 2 wpi with 20 ml of ice-cold 0.1 M PBS, followed by 20 ml of ice-cold hydrogel
857 monomer solution [4% acrylamide (Bio-Rad, #161-0140), 0.25% azo-initiator (Wako, #VA-
858 044), 4% Paraformaldehyde (Electron Microscopy Sciences, #15714-S) in PBS (Invitrogen,
859 #70011-044)]. Each spinal cord was quickly dissected, its dorsal surface longitudinally sliced
860 with attached dorsal roots, and the dorsal spinal cord placed in 20 ml of cold hydrogel in a 50 ml
861 conical tube. After 24 hours at 4oC, the tube was placed in a desiccation chamber with its lid
862 twisted open but not removed. The desiccation chamber was attached to a vacuum for 10
863 minutes, the chamber then purged with nitrogen gas, and the tube lid quickly screwed shut to
864 prevent exposure to the outside air. The 50 ml tubes were placed in a 37°C water bath for 2 hours
865 to allow for polymerization of the hydrogel and tissue. After polymerization, spinal cord was
866 transferred into a 50 ml tube with clearing solution 20 mM lithium hydroxide monohydrate
867 (Sigma-Aldrich, #254274), 200 mM boric acid (Sigma-Aldrich, #B7901), 4% SDS (Sigma-
868 Aldrich, #L3771, pH to 8.5] and placed in an incubator with agitation at 37°C. Every 24 hours
869 the clearing solution was replaced with fresh clearing solution for ~ 7 days or until the tissue had
870 completely cleared. For microscopy, tissue was submerged in FocusClear (CelExplorer Labs
871 Co., #FC-101) for 24 hours at 37°C to allow for refractive index matching. Tissue was then
872 placed in an imaging well constructed on a standard microscope slide with a thin barrier of
873 BluTack putty (Bostick, Fort Wayne, IN) sealed with a Willco-Dish **(**Ted Pella, #14032-120) and
874 Kwik-Sil (World Precision Instruments, #KWIK-SIL).
875
876 **Two-photon and widefield *in vivo* imaging**
877 Both widefield and two-photon microscope set-ups were used for repeated imaging of DR axons
878 at the DREZ in living mice, as we previously described (Skuba *et al.*, 2014). Widefield imaging
879 was performed using a fluorescence stereomicroscope (M205C, Leica Microsystems) with a fast
880 shutter and a CCD camera (ORCA-Rx2, Hamamatsu) controlled by MetaMorph software
881 (Molecular Devices). Images were acquired either as single snapshots or as multiple streams of
882 10–20 frames acquired within 30–40 msec. exposure time. In-801 focus images were then
883 selected, and an overview montage was created using Photoshop (Adobe Systems). A
884 temperature controller (ATC 1000, World Precision Instruments, Inc.) and attached heating pad
885 maintained the mouse's body temperature. For prolonged (>1 hr.) sessions, continuous inhalation
886 anesthesia was consistently delivered via a laboratory animal anesthesia system (V-1 LAAS,
887 VetEquip). 2- photon imaging was performed using an upright microscope optimized for
888 confocal and multiphoton microscopy (TCS SP5 II, Leica Microsystems). After the mouse was
889 mounted to a stereotaxic holder (SR-AM and STS-A, Narishige), imaging was performed with a
890 Spectra Physics MaiTai laser tuned to ~890 nm for 2-photon excitation of YFP. Image
891 acquisition used a 20X 0.7 NA water immersion lens controlled by Leica LAS AF software. For
892 an axon ending of interest, a Z-stack was taken with line average every 1 μm throughout the
893 entire focal area spanning 20-50 μm. Laser power and offset were adjusted to reduce background
894 noise. If necessary, alignment software (Auto Aligner, Bitplane) was used to manually align off-
895 centered optical sections. Maximum intensity projections along the Z-axis are presented as the
896 final images.

897
898 **Immunohistochemistry**
899 Two or four weeks after DR crush, mice were sacrificed by an overdose of Euthasol and
900 perfused transcardially with 0.9% saline followed by 4% paraformaldehyde (PFA) in 0.1 M PBS.
901 The spinal cords with attached DRs and DRGs were removed and examined in wholemounts to
902 exclude those tissues with poor transduction of AAV2-GFP and/or spared axons. Tissues were
903 then processed for analysis on cryostat sections or as wholemounts. For analysis on cryostat
904 sections, spinal cords were post-fixed in 4% PFA overnight at 4°C and cryoprotected in 30%
905 sucrose for 24 hr. The tissues were then embedded in M-1 Embedding Matrix (Thermo Fisher
906 Scientific, Waltham, MA), transversely sectioned at 20µm using a cryostat (Leica Microsystems,
907 Germany), and mounted directly on slides (Superfrost Plus, Fisher Scientific, Pittsburgh, PA).
908 For immunolabeling, sections were rinsed in PBS for 30 min. followed by 10 min. incubation
909 with 0.1 M glycine in PBS, and 15 min. incubation with 0.2% Triton X-100, 2% bovine serum
910 albumin (BSA) in PBS (TBP). Sections were incubated with primary antibodies overnight at
911 4°C, washed three times for 30 min. with 2% BSA in PBS, and incubated with secondary
912 antibodies for 1 hr. at room temperature. After rinsing in PBS, sections were mounted in
913 Vectashield (Vector Laboratories, Burlingame, CA) and stored 832 at –20°C until examination.
914 For wholemount immunostaining of spinal cords, spinal cords with attached DRs were post-fixed
915 in 4% PFA for 2 hr. at 4°C and the dura mater removed. The spinal cord was then rinsed with
916 PBS for 30 min., incubated for 10 min. in 0.1 M glycine in 2% BSA/PBS, and permeabilized
917 with pre-cooled methanol at –20°C for 10 min. After extensive rinsing in PBS, the spinal cord
918 was incubated with primary antibody diluted in TBP at room temperature overnight, rinsed
919 thoroughly in TBP the following day, and incubated with secondary antibodies for 2 hr. at room
920 temperature. After rinsing in PBS, a thin slice of dorsal spinal cord (~2 mm thick) with attached
921 DR stumps was cut with a microscissors and mounted on slides in Vectashield (Vector
922 Laboratories).
923
924 **Transmission and immunoelectron microscopy**
925 For transmission electron microscopy, mice were perfused transcardially with 2%
926 paraformaldehyde and 2.5% glutaraldehyde in 0.1 M Na-cacodylate buffer. Lumbar spinal cord
927 segments (L3-L6) with attached DRs were removed as one piece, mounted on agarose support,
928 and placed in the vibratome well. The most superficial longitudinal slice containing the DREZ
929 (<250 µm thickness) was cut and further processed for TEM, as previously described (Di Maio *et*
930 *al.*, 2011). For immunogold labeling of OPCs, mice were perfused with ice-cold 0.9%
931 heparinized saline followed by 4% paraformaldehyde and 0.2% glutaraldehyde in 0.1M PBS (pH
932 7.4). After 2 hr. postfixation in the same fixative at 4°C, the spinal cord segment was embedded
933 in 10% gelatin, cooled to 4°C, and a vibratome section of superficial spinal cord segment (~80
934 mm thickness) collected in PBS. The vibratome sections were then incubated with 1% sodium
935 borohydride in PBS for 30 min., followed by permeabilization with 0.1% Triton-X-100 in PBS
936 for 20 min. at 4°C. The sections were blocked with blocking solution (1% BSA, 3% NGS, 0.04%
937 Triton-X-100 in PBS) for 30 min. and incubated with guinea pig anti-NG2 antibody (1:500, a
938 gift from Dr. Dwight Bergles, Johns Hopkins University) diluted with blocking buffer for 24-48
939 hr. at 4°C. After rinsing, sections were incubated with 10 nm gold-conjugated goat anti-guinea
940 pig IgG (1:200, Electron Microscopy Sciences, #25329) in blocking buffer for 3 hr. at room
941 temperature. After rinsing, sections were post-fixed in 2% glutaraldehyde in PBS for 10 min.
942 Silver enhancement was then performed in the dark with the HQ Silver Kit (Nanoprobes, NY) as

943 directed by the manufacturer. Sections were post-fixed again with 1% osmium tetroxide in PBS
944 for 10 min. and then incubated with 2% uranyl acetate in ddH2O 863 for 10 min. Sections were
945 then dehydrated in an ascending ethanol series, followed by acetone series, and finally infiltrated
946 with Araldite 502 Embed 812 resin. After polymerization, serial ultrathin sections (60–70 nm)
947 were cut and mounted on Pioloform-coated slot grids. They were observed with a JEOL 1010
948 electron microscope at the Electron Microscopy Resource Lab, University of Pennsylvania.
949
950 **Western blotting**
951 The dura was removed from the spinal cord, which was then snap-frozen in liquid nitrogen and
952 stored at -80oC. Spinal cords were lysed in RIPA buffer (25 mM Tris pH 7.5, 150 mM NaCl, 1%
953 Triton X-100, 0.5% sodium deoxycholate, 1 mM EDTA, 0.1% SDS). Lysis was for 40 min. on
954 ice, followed by microcentrifugation at 14,000 rpm for 20 min. Protein concentration was
955 determined using the BCA assay (ThermoFisher). Primary antibodies were used at the following
956 concentrations for Western blots: rabbit anti-NG2 (Millipore, AB5320; 1:500), mouse anti-β-
957 actin (Sigma, A5441; 1:1,000), and rat anti-PDGFRα (BD Biosciences, 558774; 1:500).
958 Secondary antibodies for Western blots were HRP-conjugated goat anti-rabbit antibody (Santa
959 Cruz, SC2030; 1:10,000), HRP-conjugated goat anti-mouse antibody (Jackson ImmunoResearch
960 Laboratories, 115-035-174, 1:10,000), or HRP-conjugated goat anti-rat antibody (Jackson
961 ImmunoResearch Laboratories, 112-035-003; 1:10,000). Blots were developed using ECL, ECL
962 Plus (GE Healthcare, RPN2236).
963
964 **Antibodies for immunohistochemistry**
965 Primary antibodies were used at the following concentrations for immunohistochemistry: rabbit
966 anti-glial fibrillary acidic protein (GFAP, N1506; 1:500), mouse anti-GFAP (Sigma-Aldrich,
967 G3893; 1:500), goat anti-myelin oligodendrocyte glycoprotein (MOG; R&D Systems, AF2439;
968 1:200), mouse anti-SC2E (Cosmo Bio Co., CAC-GU01-M01AS-A; 1:10,000), goat anti-
969 p75NGFR (Neuromics, GT15057; 1:500), rat anti-ED1 (AbD serotec, MCA1957; 1:400), rabbit
970 anti-CGRP (Peninsula Lab., T-4032; 1:2,000), rabbit anti-NF200 (Sigma-Aldrich, N4142,
971 1:500), mouse anti-SV2 (Developmental Studies Hybridoma Bank, SV2; 1:10), guinea pig anti-
972 NG2 (1:500, a gift from Dr. Dwight Bergles, Johns Hopkins University), rat anti-PDGFRα (BD
973 Biosciences, 558774; 1:500), mouse anti adenomatous polyposis coli antigen (APC; clone CC1;
974 Millipore, OP80- 100UG; 1:100), rabbit anti-PDGFRα (abcam, ab203491; 1:500), mouse anti-
975 PDGFRβ (abcam, ab69506; 1:500), mouse anti-CS56 (Sigma-Aldrich, C8035 1:1,000), goat
976 anti-CD31/PECAM (R&D Systems, AF3628; 1:200), rabbit anti-vimentin (abcam, ab92547;
977 1:1,000). Secondary antibodies were FITC conjugated goat anti-mouse IgG (Invitrogen, A10530;
978 1:400), Alexa-Fluor 568-conjugated goat anti-894 mouse IgG (Invitrogen, A21124; 1:400),
979 Alexa-Fluor 488-conjugated goat anti-rabbit IgG (Invitrogen, A11034; 1:400), Alexa-Flour 568
980 conjugated goat anti-rabbit IgG (Invitrogen, A11011; 1:400), Alexa-Flour 546 conjugated
981 donkey anti-rabbit IgG (Invitrogen, A10040; 1:400), Alexa-Fluor 647-conjugated donkey anti
982 rabbit IgG (Invitrogen, A31573; 1:400), Alexa-Fluor 647-conjugated goat anti-rabbit IgG
983 (Invitrogen, A21244; 1:400), Alexa-Flour 488 conjugated donkey anti-goat IgG (Invitrogen,
984 A11055; 1:400), rhodamine (TRITC)-conjugated donkey anti-rat IgG (Jackson ImmunoResearch
985 Laboratories, 712-025-150; 1:400), Cy3-conjugated donkey anti-guinea pig IgG (Jackson
986 ImmunoResearch Laboratories, 706-166-148; 1:400), and Dye 647-conjugated donkey anti
987 guinea pig IgG (Jackson ImmunoResearch Laboratories, 706-606-148; 1:400).
988

989 **OPC purification and co-culture with Percoll-purified DRG neurons**
990 OPCs were isolated from P16-P18 C57BL/6 mice by immunopanning as previously described
991 (Cahoy et al., 2008). Dissociated spinal cords were resuspended in panning buffer. To deplete
992 microglia, the cell suspension was sequentially panned on two BSL1 panning plates (Vector
993 Laboratories, #L1100). To purify OPCs, the cell suspension was then incubated on two PDGFRα
994 plates coated with rat anti-PDGFRα IgG (BD Biosciences, 558774; 1:500). The adherent cells
995 were washed with PBS to remove all antigen-negative nonadherent cells. The adherent cells were
996 trypsinized and plated onto poly-D-lysine (PDL)-coated plates. The cultures were maintained
997 under proliferating conditions by the addition of PDGFAA (Sigma, SRP3228; 10ng/ml) and
998 bFGF (Sigma, SRP4038; 20 ng/ml) to the serum-free medium (DMEM, B27 supplement, 1X
999 Sato supplement, 1X Trace Elements B, 10 ng/ml d-biotin, 2 mM Glutamine, 1 mM sodium
1000 pyruvate, 5 ug/ml insulin, 5 μg/ml N-acetyl-L-cysteine, 500 mM Forskolin, 100 U/ml Penicillin
1001 streptomycin). Most cells (>95%) expressed OPC markers Olig2, NG2, and PDGFRα. After 5
1002 days of incubation, percoll-purified DRG neurons were applied to cultured OPCs and cocultured
1003 for 5 days. For isolating DRG neurons, ~20 DRGs were removed from adult C57BL/6 mice and
1004 then dissociated in 1 ug/ml collagenase A and 2.4 U/ml dispase II. The dissociated DRGs were
1005 added to a two-layered Percoll gradient (12.5% Percoll layered over 28% Percoll solution with
1006 DMEM) and then subjected to density-gradient centrifugation. The interphase fraction was
1007 subsequently removed, spun, and resuspended in 20 μl of DMEM. A small amount of the cell
1008 suspension (<5 μl) was added sparingly to cultured OPCs in the OPC proliferating medium. The
1009 cocultures were incubated in 5% CO2 at 37oC for 5 days.
1010
1011 **Calcium imaging**
1012 Calcium imaging was performed using fura-2-based microfluorimetry and imaging analysis as
1013 we previously described (Dou et al., 2018). OPC-DRG neuron cocultures on coverslips were
1014 loaded with 4 μM of fura-2AM (Life Technologies, Grand Island, NY) for 30 min. at room
1015 temperature in HBSS, washed, and further incubated in normal bath solution (Tyrode's; 140 mM
1016 NaCl, 5 KCl mM, 2 CaCl2 mM, 1 MgCl2 mM, 10 HEPES mM, and 5.6 mM glucose).
1017 Coverslips were mounted in a small perfusion chamber (Warner Instruments, Model RC-25) and
1018 continuously perfused at 5–7 ml/min with Tyrode's solution. 100 nM capsaicin in Tyrode's
1019 solution, with or without 20μM CNQX and 10μM AP5, was locally infused for 20 sec., using a
1020 glass electrode (~500 μm ID) positioned ~1.0 mm away from cells. Images were acquired at 3 s.
1021 intervals at room temperature using an Olympus inverted microscope equipped with a CCD
1022 camera (Hamamatsu, ORCA-03G). The fluorescence images were recorded and analyzed using
1023 the software MetaFluor 7.7.9 (Molecular Devices). The fluorescence ratio was determined as the
1024 fluorescence intensities excited at 340 and 380 nm with background subtraction.
1025
1026 **Quantification and statistical analysis**
1027 **Fluorescence microscopy, cell counting, and densitometric analysis**
1028 Z-stack fluorescent images were acquired on a Zeiss Axio Imager widefield microscope or on a
1029 Leica SP8 confocal microscope from 20μm serial transverse sections of spinal cords. Acquisition
1030 parameters were kept constant between different groups. Acquired images were merged using
1031 Imaris (Bitplane, Windsor, CT) and processed in Adobe Photoshop with minimal manipulations
1032 of brightness and contrast (Adobe Inc, San Jose, CA). For counting Ki67, Olig2, Iba1, ED1, and
1033 Sox10+ cells, 3 to 6 representative, non-adjacent sections taken from spinal cord segments of
1034 each mouse (n=3-6 per cohort) were carefully selected. Cell counting was performed blindly

using ImageJ/Fiji (NIH). Immunoreactive cells were manually counted in ipsilateral regions of dorsal lateral funiculus, dorsal root, or dorsal spinal cord, and then averaged by the number of evaluated sections and animals. For comparative analysis of OPC ablation, CSPG deletion, GFAP, and p75 immunoreactivity, images were converted to grayscale, subthresholded to the background, and calculated using ImageJ/Fiji (NIH). Intensity was defined as the average gray value obtained from all pixels within the region of interest 955 above background. Data are presented as the mean fluorescence intensities (MFI) in each region of interest, calculated by subtracting the mean value of randomly selected background regions lacking immunoreactivity of interest.

**Analysis of axon regeneration across the DREZ**

The DREZ was defined as the ~100µm wide CNS territory beyond the boundary between the CNS and PNS. The yellow dotted lines (e.g., Figure 3A) denote the boundary (termed also borderline or border), demarcated by GFAP immunolabeling of astrocytic processes that extend peripherally. When GFAP was not immunolabeled, the borderline was identified based on the greater abundance of cell nuclei in the PNS than CNS (Zhai *et al.*, 2021). For comparative evaluation of regeneration, we considered that an axon penetrated the DREZ when it extended at least 100µm beyond the borderline. For quantitative analysis, digital images were captured from 3 to 6 representative, non-adjacent sections taken from spinal cord segments of each mouse (n = 3–6 mice per cohort). A raw image was converted to a binary image using ImageJ with a threshold that appropriately separated GFP and background fluorescence. Lines were drawn at 100µm before the borderline in the PNS, at the borderline, and at 100µm intervals into CNS territory. The number of intersections of GFP+ axons at these distances was counted. The number of axons that crossed the border was normalized by the number of GFP+ axons counted at 100µm before the borderline in the PNS, and then averaged by the number of evaluated sections and animals. This quantification resulted in the 'axon number index' that indicated the relative number and distance of axons that regenerated into the CNS or spinal cord.

**Statistical analysis**

All statistical analyses were performed using PRISM 9.0 (GraphPad). Statistical analysis was done using the two-sample Mann-Whitney test or unpaired t-test for two-group comparisons, and analysis of variance (ANOVA) with Tukey's or Sidak's test for multiple comparisons, as appropriate. All data were presented as mean ± SEM or SD as indicated in the figure legend. A p-value of 0.05 or less was considered statistically significant.

## SUPPLEMENTAL INFORMATION

Supplemental figures and figure legends – 7 Supplemental figures

Supplemental experimental procedures - TBD

## REFERENCES

1. Kaiser, R., Waldauf, P., Ullas, G., and Krajcová, A. (2020). Epidemiology, etiology, and types of severe adult brachial plexus injuries requiring surgical repair: systematic review and meta-analysis. Neurosurg Rev *43*, 443-452. 10.1007/s10143-018-1009-2.

1081 2. Varadarajan, S.G., Hunyara, J.L., Hamilton, N.R., Kolodkin, A.L., and Huberman, A.D.
1082 (2022). Central nervous system regeneration. Cell *185*, 77-94.
1083 10.1016/j.cell.2021.10.029.

1084 3. He, Z., and Jin, Y. (2016). Intrinsic Control of Axon Regeneration. Neuron *90*, 437-451.
1085 10.1016/j.neuron.2016.04.022.

1086 4. Zheng, B., and Tuszynski, M.H. (2023). Regulation of axonal regeneration after
1087 mammalian spinal cord injury. Nature reviews. Molecular cell biology. 10.1038/s41580-
1088 022-00562-y.

1089 5. Chong, M.S., Woolf, C.J., Haque, N.S., and Anderson, P.N. (1999). Axonal regeneration
1090 from injured dorsal roots into the spinal cord of adult rats. J Comp Neurol *410*, 42-54.
1091 10.1002/(SICI)1096-9861(19990719)410:1<42::AID-CNE5>3.0.CO;2-F [pii].

1092 6. Di Maio, A., Skuba, A., Himes, B.T., Bhagat, S.L., Hyun, J.K., Tessler, A., Bishop, D.,
1093 and Son, Y.J. (2011). In Vivo Imaging of Dorsal Root Regeneration: Rapid
1094 Immobilization and Presynaptic Differentiation at the CNS/PNS Border. The Journal of
1095 neuroscience : the official journal of the Society for Neuroscience *31*, 4569-4582.
1096 31/12/4569 [pii] 10.1523/JNEUROSCI.4638-10.2011.

1097 7. Smith, G.M., Falone, A.E., and Frank, E. (2012). Sensory axon regeneration: rebuilding
1098 functional connections in the spinal cord. Trends Neurosci *35*, 156-163.
1099 10.1016/j.tins.2011.10.006.

1100 8. Mar, F.M., Simões, A.R., Rodrigo, I.S., and Sousa, M.M. (2016). Inhibitory Injury
1101 Signaling Represses Axon Regeneration After Dorsal Root Injury. Molecular
1102 neurobiology *53*, 4596-4605. 10.1007/s12035-015-9397-6.

1103 9. Zhai, J., Kim, H., Han, S.B., Manire, M., Yoo, R., Pang, S., Smith, G.M., and Son, Y.J.
1104 (2021). Co-targeting myelin inhibitors and CSPGs markedly enhances regeneration of
1105 GDNF-stimulated, but not conditioning-lesioned, sensory axons into the spinal cord.
1106 eLife *10*. 10.7554/eLife.63050.

1107 10. Blanquie, O., and Bradke, F. (2018). Cytoskeleton dynamics in axon regeneration.
1108 Current opinion in neurobiology *51*, 60-69. 10.1016/j.conb.2018.02.024.

1109 11. Hill, C.E. (2017). A view from the ending: Axonal dieback and regeneration following
1110 SCI. Neuroscience letters *652*, 11-24. 10.1016/j.neulet.2016.11.002.

1111 12. Son, Y.J. (2015). Synapsing with NG2 cells (polydendrocytes), unappreciated barrier to
1112 axon regeneration? Neural regeneration research *10*, 346-348. 10.4103/1673-
1113 5374.153672.

1114 13. Bergles, D.E., Roberts, J.D., Somogyi, P., and Jahr, C.E. (2000). Glutamatergic synapses
1115 on oligodendrocyte precursor cells in the hippocampus. Nature *405*, 187-191.
1116 10.1038/35012083.

1117 14. Mount, C.W., Yalçın, B., Cunliffe-Koehler, K., Sundaresh, S., and Monje, M. (2019).
1118 Monosynaptic tracing maps brain-wide afferent oligodendrocyte precursor cell
1119 connectivity. eLife *8*. 10.7554/eLife.49291.

1120 15. Osterstock, G., Le Bras, B., Arulkandarajah, K.H., Le Corronc, H., Czarnecki, A.,
1121 Mouffle, C., Bullier, E., Legendre, P., and Mangin, J.M. (2018). Axoglial synapses are
1122 formed onto pioneer oligodendrocyte precursor cells at the onset of spinal cord
1123 gliogenesis. Glia *66*, 1678-1694. 10.1002/glia.23331.

1124 16. Li, M., Shibata, A., Li, C., Braun, P.E., McKerracher, L., Roder, J., Kater, S.B., and
1125 David, S. (1996). Myelin-associated glycoprotein inhibits neurite/axon growth and causes
1126 growth cone collapse. J Neurosci Res *46*, 404-414. 10.1002/(SICI)1097-
1127 4547(19961115)46:4<404::AID-JNR2>3.0.CO;2-K [pii]

1128 10.1002/(SICI)1097-4547(19961115)46:4<404::AID-JNR2>3.0.CO;2-K.

1129 17. Tom, V.J., Steinmetz, M.P., Miller, J.H., Doller, C.M., and Silver, J. (2004). Studies on
1130 the development and behavior of the dystrophic growth cone, the hallmark of
1131 regeneration failure, in an in vitro model of the glial scar and after spinal cord injury. The
1132 Journal of neuroscience : the official journal of the Society for Neuroscience *24*, 6531-
1133 6539. 10.1523/JNEUROSCI.0994-04.2004 24/29/6531 [pii].

1134 18. Cregg, J.M., DePaul, M.A., Filous, A.R., Lang, B.T., Tran, A., and Silver, J. (2014).
1135 Functional regeneration beyond the glial scar. Experimental neurology *253*, 197-207.
1136 10.1016/j.expneurol.2013.12.024.

1137 19. Skuba, A., Manire, M.A., Kim, H., Han, S.B., and Son, Y.J. (2014). Time-lapse in vivo
1138 imaging of dorsal root nerve regeneration in mice. Methods Mol Biol *1162*, 219-232.
1139 10.1007/978-1-4939-0777-9_18.

1140 20. Feng, G.P., Mellor, R.H., Bernstein, M., Keller-Peck, C., Nguyen, Q.T., Wallace, M.,
1141 Nerbonne, J.M., Lichtman, J.W., and Sanes, J.R. (2000). Imaging neuronal subsets in
1142 transgenic mice expressing multiple spectral variants of GFP. Neuron *28*, 41-51.
1143 10.1016/s0896-6273(00)00084-2.

1144 21. Busch, S.A., Horn, K.P., Silver, D.J., and Silver, J. (2009). Overcoming macrophage-
1145 mediated axonal dieback following CNS injury. The Journal of neuroscience : the official
1146 journal of the Society for Neuroscience *29*, 9967-9976. 29/32/9967 [pii]
1147 10.1523/JNEUROSCI.1151-09.2009.

1148 22. Evans, T.A., Barkauskas, D.S., Myers, J.T., Hare, E.G., You, J.Q., Ransohoff, R.M.,
1149 Huang, A.Y., and Silver, J. (2014). High-resolution intravital imaging reveals that blood-
1150 derived macrophages but not resident microglia facilitate secondary axonal dieback in
1151 traumatic spinal cord injury. Experimental neurology *254*, 109-120.
1152 10.1016/j.expneurol.2014.01.013.

1153 23. Partyka, P.P., Jin, Y., Bouyer, J., DaSilva, A., Godsey, G.A., Nagele, R.G., Fischer, I.,
1154 and Galie, P.A. (2019). Harnessing neurovascular interaction to guide axon growth.
1155 Scientific reports *9*, 2190. 10.1038/s41598-019-38558-y.

1156 24. Hesp, Z.C., Yoseph, R.Y., Suzuki, R., Jukkola, P., Wilson, C., Nishiyama, A., and
1157 McTigue, D.M. (2018). Proliferating NG2-Cell-Dependent Angiogenesis and Scar
1158 Formation Alter Axon Growth and Functional Recovery After Spinal Cord Injury in
1159 Mice. The Journal of neuroscience : the official journal of the Society for Neuroscience
1160 *38*, 1366-1382. 10.1523/jneurosci.3953-16.2017.

1161 25. McTigue, D.M., Tripathi, R., and Wei, P. (2006). NG2 colocalizes with axons and is
1162 expressed by a mixed cell population in spinal cord lesions. J Neuropathol Exp Neurol
1163 *65*, 406-420. 10.1097/01.jnen.0000218447.32320.52 00005072-200604000-00010 [pii].

1164 26. Vanlandewijck, M., He, L., Mäe, M.A., Andrae, J., Ando, K., Del Gaudio, F., Nahar, K.,
1165 Lebouvier, T., Laviña, B., Gouveia, L., et al. (2018). A molecular atlas of cell types and
1166 zonation in the brain vasculature. Nature *554*, 475-480. 10.1038/nature25739.

1167 27. Marques, S., Zeisel, A., Codeluppi, S., van Bruggen, D., Mendanha Falcão, A., Xiao, L.,
1168 Li, H., Häring, M., Hochgerner, H., Romanov, R.A., et al. (2016). Oligodendrocyte
1169 heterogeneity in the mouse juvenile and adult central nervous system. Science *352*, 1326-
1170 1329. doi:10.1126/science.aaf6463.

1171 28. Tomita, Y., Horiuchi, K., Kano, K., Tatsukawa, T., Matsuo, R., Hayasaka, T., Yoshida,
1172 Y., Kabara, M., Yasuda, S., Nakajima, K., et al. (2019). Ninjurin 1 mediates peripheral
1173 nerve regeneration through Schwann cell maturation of NG2-positive cells. Biochem
1174 Biophys Res Commun *519*, 462-468. 10.1016/j.bbrc.2019.09.007.

1175 29. Richard, L., Védrenne, N., Vallat, J.M., and Funalot, B. (2014). Characterization of
1176 Endoneurial Fibroblast-like Cells from Human and Rat Peripheral Nerves. The journal of
1177 histochemistry and cytochemistry : official journal of the Histochemistry Society *62*, 424-
1178 435. 10.1369/0022155414530994.

1179 30. Bergles, D.E., and Richardson, W.D. (2015). Oligodendrocyte Development and
1180 Plasticity. Cold Spring Harb Perspect Biol *8*, a020453. 10.1101/cshperspect.a020453.

1181 31. Kula, B., Chen, T.J., and Kukley, M. (2019). Glutamatergic signaling between neurons
1182 and oligodendrocyte lineage cells: Is it synaptic or non-synaptic? Glia *67*, 2071-2091.
1183 10.1002/glia.23617.

1184 32. Tamburini, E., Dallatomasina, A., Quartararo, J., Cortelazzi, B., Mangieri, D., Lazzaretti,
1185 M., and Perris, R. (2019). Structural deciphering of the NG2/CSPG4 proteoglycan
1186 multifunctionality. FASEB journal : official publication of the Federation of American
1187 Societies for Experimental Biology *33*, 3112-3128. 10.1096/fj.201801670R.

1188 33. Carlstedt, T., Dalsgaard, C.J., and Molander, C. (1987). Regrowth of lesioned dorsal root
1189 nerve fibers into the spinal cord of neonatal rats. Neuroscience letters *74*, 14-18.

1190 34. Golding, J.P., Shewan, D., Berry, M., and Cohen, J. (1996). An in vitro model of the rat
1191 dorsal root entry zone reveals developmental changes in the extent of sensory axon
1192 growth into the spinal cord. Mol Cell Neurosci *7*, 191-203. 10.1006/mcne.1996.0015.

1193 35. Szallasi, A., and Blumberg, P.M. (1999). Vanilloid (Capsaicin) receptors and
1194 mechanisms. Pharmacol Rev *51*, 159-212.

1195 36. Akay, L.A., Effenberger, A.H., and Tsai, L.H. (2021). Cell of all trades: oligodendrocyte
1196 precursor cells in synaptic, vascular, and immune function. Genes Dev *35*, 180-198.
1197 10.1101/gad.344218.120.

1198 37. Sun, W., Matthews, E.A., Nicolas, V., Schoch, S., and Dietrich, D. (2016). NG2 glial
1199 cells integrate synaptic input in global and dendritic calcium signals. eLife *5*.
1200 10.7554/eLife.16262.

1201 38. Filous, A.R., Tran, A., Howell, C.J., Busch, S.A., Evans, T.A., Stallcup, W.B., Kang,
1202 S.H., Bergles, D.E., Lee, S.I., Levine, J.M., and Silver, J. (2014). Entrapment via
1203 synaptic-like connections between NG2 proteoglycan+ cells and dystrophic axons in the
1204 lesion plays a role in regeneration failure after spinal cord injury. The Journal of
1205 neuroscience : the official journal of the Society for Neuroscience *34*, 16369-16384.
1206 10.1523/jneurosci.1309-14.2014.

1207 39. Hughes, E.G., Kang, S.H., Fukaya, M., and Bergles, D.E. (2013). Oligodendrocyte
1208 progenitors balance growth with self-repulsion to achieve homeostasis in the adult brain.
1209 Nat Neurosci *16*, 668-676. 10.1038/nn.3390.

1210 40. Birey, F., and Aguirre, A. (2015). Age-Dependent Netrin-1 Signaling Regulates NG2+
1211 Glial Cell Spatial Homeostasis in Normal Adult Gray Matter. The Journal of
1212 neuroscience : the official journal of the Society for Neuroscience *35*, 6946-6951.
1213 10.1523/jneurosci.0356-15.2015.

1214 41. Brockschnieder, D., Lappe-Siefke, C., Goebbels, S., Boesl, M.R., Nave, K.A., and
1215 Riethmacher, D. (2004). Cell depletion due to diphtheria toxin fragment A after Cre-
1216 mediated recombination. Mol Cell Biol *24*, 7636-7642. 10.1128/mcb.24.17.7636-
1217 7642.2004.

1218 42. Birey, F., Kloc, M., Chavali, M., Hussein, I., Wilson, M., Christoffel, D.J., Chen, T.,
1219 Frohman, M.A., Robinson, J.K., Russo, S.J., et al. (2019). Genetic and Stress-Induced
1220 Loss of NG2 Glia Triggers Emergence of Depressive-like Behaviors through Reduced
1221 Secretion of FGF2. Neuron *104*, 825-826. 10.1016/j.neuron.2019.11.005.

1222 43. Djogo, T., Robins, S.C., Schneider, S., Kryzskaya, D., Liu, X., Mingay, A., Gillon, C.J.,
1223 Kim, J.H., Storch, K.F., Boehm, U., et al. (2016). Adult NG2-Glia Are Required for
1224 Median Eminence-Mediated Leptin Sensing and Body Weight Control. Cell Metab *23*,
1225 797-810. 10.1016/j.cmet.2016.04.013.

1226 44. Xing, Y.L., Poh, J., Chuang, B.H.A., Moradi, K., Mitew, S., Richardson, W.D.,
1227 Kilpatrick, T.J., Osanai, Y., and Merson, T.D. (2023). High-efficiency pharmacogenetic

1228 ablation of oligodendrocyte progenitor cells in the adult mouse CNS. Cell reports
1229 methods *3*, 100414. 10.1016/j.crmeth.2023.100414.

1230 45. Marques, S., Zeisel, A., Codeluppi, S., van Bruggen, D., Mendanha Falcão, A., Xiao, L.,
1231 Li, H., Häring, M., Hochgerner, H., Romanov, R.A., et al. (2016). Oligodendrocyte
1232 heterogeneity in the mouse juvenile and adult central nervous system. Science *352*, 1326-
1233 1329. 10.1126/science.aaf6463.

1234 46. Lovatt, D., Tamburino, A., Krasowska-Zoladek, A., Sanoja, R., Li, L., Peterson, V.,
1235 Wang, X., and Uslaner, J. (2022). scRNA-seq generates a molecular map of emerging
1236 cell subtypes after sciatic nerve injury in rats. Communications biology *5*, 1105.
1237 10.1038/s42003-022-03970-0.

1238 47. Weinrauch, Y., and Zychlinsky, A. (1999). The induction of apoptosis by bacterial
1239 pathogens. Annu Rev Microbiol *53*, 155-187. 10.1146/annurev.micro.53.1.155.

1240 48. Labbé, K., and Saleh, M. (2008). Cell death in the host response to infection. Cell death
1241 and differentiation *15*, 1339-1349. 10.1038/cdd.2008.91.

1242 49. Xiao, Y., Petrucco, L., Hoodless, L.J., Portugues, R., and Czopka, T. (2022).
1243 Oligodendrocyte precursor cells sculpt the visual system by regulating axonal
1244 remodeling. Nat Neurosci *25*, 280-284. 10.1038/s41593-022-01023-7.

1245 50. Liu, Y., and Aguzzi, A. (2020). NG2 glia are required for maintaining microglia
1246 homeostatic state. Glia *68*, 345-355. 10.1002/glia.23721.

1247 51. Afshari, F.T., Kwok, J.C., and Fawcett, J.W. (2010). Astrocyte-produced ephrins inhibit
1248 schwann cell migration via VAV2 signaling. The Journal of neuroscience : the official
1249 journal of the Society for Neuroscience *30*, 4246-4255. 30/12/4246 [pii]
1250 10.1523/JNEUROSCI.3351-09.2010.

1251 52. Gerber, D., Pereira, J.A., Gerber, J., Tan, G., Dimitrieva, S., Yángüez, E., and Suter, U.
1252 (2021). Transcriptional profiling of mouse peripheral nerves to the single-cell level to
1253 build a sciatic nerve ATlas (SNAT). eLife *10*. 10.7554/eLife.58591.

1254 53. Tran, A.P., Warren, P.M., and Silver, J. (2018). The Biology of Regeneration Failure and
1255 Success After Spinal Cord Injury. Physiol Rev *98*, 881-917.
1256 10.1152/physrev.00017.2017.

1257 54. Liuzzi, F.J., and Lasek, R.J. (1987). Astrocytes block axonal regeneration in mammals by
1258 activating the physiological stop pathway. Science *237*, 642-645.

1259 55. Carlstedt, T. (1985). Regenerating axons form nerve terminals at astrocytes. Brain Res
1260 *347*, 188-191. 0006-8993(85)90911-4 [pii].

1261 56. Vargas, M.E., and Barres, B.A. (2007). Why is Wallerian degeneration in the CNS so
1262 slow? Annu Rev Neurosci *30*, 153-179. 10.1146/annurev.neuro.30.051606.094354.

1263 57. Dorrier, C.E., Aran, D., Haenelt, E.A., Sheehy, R.N., Hoi, K.K., Pintarić, L., Chen, Y.,
1264 Lizama, C.O., Cautivo, K.M., Weiner, G.A., et al. (2021). CNS fibroblasts form a fibrotic
1265 scar in response to immune cell infiltration. Nat Neurosci *24*, 234-244. 10.1038/s41593-
1266 020-00770-9.

1267 58. Wiliams, R.R., and Bunge, M.B. (2012). Schwann cell transplantation: a repair strategy
1268 for spinal cord injury? Prog Brain Res *201*, 295-312. 10.1016/b978-0-444-59544-
1269 7.00014-7.

1270 59. Warren, P.M., Andrews, M.R., Smith, M., Bartus, K., Bradbury, E.J., Verhaagen, J.,
1271 Fawcett, J.W., and Kwok, J.C.F. (2020). Secretion of a mammalian chondroitinase ABC
1272 aids glial integration at PNS/CNS boundaries. Scientific reports *10*, 11262.
1273 10.1038/s41598-020-67526-0.

1274 60. Li, Y., Carlstedt, T., Berthold, C.H., and Raisman, G. (2004). Interaction of transplanted
1275 olfactory-ensheathing cells and host astrocytic processes provides a bridge for axons to
1276 regenerate across the dorsal root entry zone. Experimental neurology *188*, 300-308.
1277 10.1016/j.expneurol.2004.04.021.

1278 61. Zukor, K., Belin, S., Wang, C., Keelan, N., Wang, X., and He, Z. (2013). Short hairpin
1279 RNA against PTEN enhances regenerative growth of corticospinal tract axons after spinal
1280 cord injury. The Journal of neuroscience : the official journal of the Society for
1281 Neuroscience *33*, 15350-15361. 10.1523/jneurosci.2510-13.2013.

1282 62. Fraher, J. (2002). Axons and glial interfaces: ultrastructural studies. Journal of anatomy
1283 *200*, 415-430. 10.1046/j.1469-7580.2002.00037.x.

1284 63. Friedman, H.V., Bresler, T., Garner, C.C., and Ziv, N.E. (2000). Assembly of new
1285 individual excitatory synapses: time course and temporal order of synaptic molecule
1286 recruitment. Neuron *27*, 57-69. 10.1016/s0896-6273(00)00009-x.

1287 64. Lucido, A.L., Suarez Sanchez, F., Thostrup, P., Kwiatkowski, A.V., Leal-Ortiz, S.,
1288 Gopalakrishnan, G., Liazoghli, D., Belkaid, W., Lennox, R.B., Grutter, P., et al. (2009).
1289 Rapid assembly of functional presynaptic boutons triggered by adhesive contacts. The
1290 Journal of neuroscience : the official journal of the Society for Neuroscience *29*, 12449-
1291 12466. 10.1523/jneurosci.1381-09.2009.

1292 65. Kukley, M., Capetillo-Zarate, E., and Dietrich, D. (2007). Vesicular glutamate release
1293 from axons in white matter. Nat Neurosci *10*, 311-320. 10.1038/nn1850.

1294 66. Kukley, M., Kiladze, M., Tognatta, R., Hans, M., Swandulla, D., Schramm, J., and
1295 Dietrich, D. (2008). Glial cells are born with synapses. FASEB journal : official
1296 publication of the Federation of American Societies for Experimental Biology *22*, 2957-
1297 2969. 10.1096/fj.07-090985.

1298 67. Ge, W.P., Zhou, W., Luo, Q., Jan, L.Y., and Jan, Y.N. (2009). Dividing glial cells
1299 maintain differentiated properties including complex morphology and functional

1300 synapses. Proceedings of the National Academy of Sciences of the United States of
1301 America *106*, 328-333. 10.1073/pnas.0811353106.

1302 68. Tedeschi, A., Dupraz, S., Laskowski, C.J., Xue, J., Ulas, T., Beyer, M., Schultze, J.L.,
1303 and Bradke, F. (2016). The Calcium Channel Subunit Alpha2delta2 Suppresses Axon
1304 Regeneration in the Adult CNS. Neuron *92*, 419-434. 10.1016/j.neuron.2016.09.026.

1305 69. Hilton, B.J., Husch, A., Schaffran, B., Lin, T.C., Burnside, E.R., Dupraz, S., Schelski,
1306 M., Kim, J., Müller, J.A., Schoch, S., et al. (2022). An active vesicle priming machinery
1307 suppresses axon regeneration upon adult CNS injury. Neuron *110*, 51-69.e57.
1308 10.1016/j.neuron.2021.10.007.

1309 70. Lorenzana, A.O., Lee, J.K., Mui, M., Chang, A., and Zheng, B. (2015). A surviving intact
1310 branch stabilizes remaining axon architecture after injury as revealed by in vivo imaging
1311 in the mouse spinal cord. Neuron *86*, 947-954. 10.1016/j.neuron.2015.03.061.

1312 71. Passlick, S., Trotter, J., Seifert, G., Steinhäuser, C., and Jabs, R. (2016). The NG2 Protein
1313 Is Not Required for Glutamatergic Neuron-NG2 Cell Synaptic Signaling. Cereb Cortex
1314 *26*, 51-57. 10.1093/cercor/bhu171.

1315 72. Hughes, A.N., and Appel, B. (2019). Oligodendrocytes express synaptic proteins that
1316 modulate myelin sheath formation. Nat Commun *10*, 4125. 10.1038/s41467-019-12059-
1317 y.

1318 73. Südhof, T.C. (2018). Towards an Understanding of Synapse Formation. Neuron *100*,
1319 276-293. 10.1016/j.neuron.2018.09.040.

1320 74. Pinto, M.J., and Almeida, R.D. (2016). Puzzling out presynaptic differentiation. J
1321 Neurochem *139*, 921-942. 10.1111/jnc.13702.

1322 75. Wu, D., Jin, Y., Shapiro, T.M., Hinduja, A., Baas, P.W., and Tom, V.J. (2020). Chronic
1323 neuronal activation increases dynamic microtubules to enhance functional axon
1324 regeneration after dorsal root crush injury. Nat Commun *11*, 6131. 10.1038/s41467-020-
1325 19914-3.

1326 76. Verhage, M., Maia, A.S., Plomp, J.J., Brussaard, A.B., Heeroma, J.H., Vermeer, H.,
1327 Toonen, R.F., Hammer, R.E., van den Berg, T.K., Missler, M., et al. (2000). Synaptic
1328 assembly of the brain in the absence of neurotransmitter secretion. Science *287*, 864-869.
1329 10.1126/science.287.5454.864.

1330 77. Held, R.G., Liu, C., Ma, K., Ramsey, A.M., Tarr, T.B., De Nola, G., Wang, S.S.H.,
1331 Wang, J., van den Maagdenberg, A., Schneider, T., et al. (2020). Synapse and Active
1332 Zone Assembly in the Absence of Presynaptic Ca(2+) Channels and Ca(2+) Entry.
1333 Neuron *107*, 667-683.e669. 10.1016/j.neuron.2020.05.032.

1334 78. Andreae, L.C., and Burrone, J. (2014). The role of neuronal activity and transmitter
1335 release on synapse formation. Current opinion in neurobiology *27*, 47-52.
1336 10.1016/j.conb.2014.02.008.

1337 79. Skaper, S.D. (2019). Oligodendrocyte precursor cells as a therapeutic target for
1338 demyelinating diseases. Prog Brain Res *245*, 119-144. 10.1016/bs.pbr.2019.03.013.

1339
1340

A

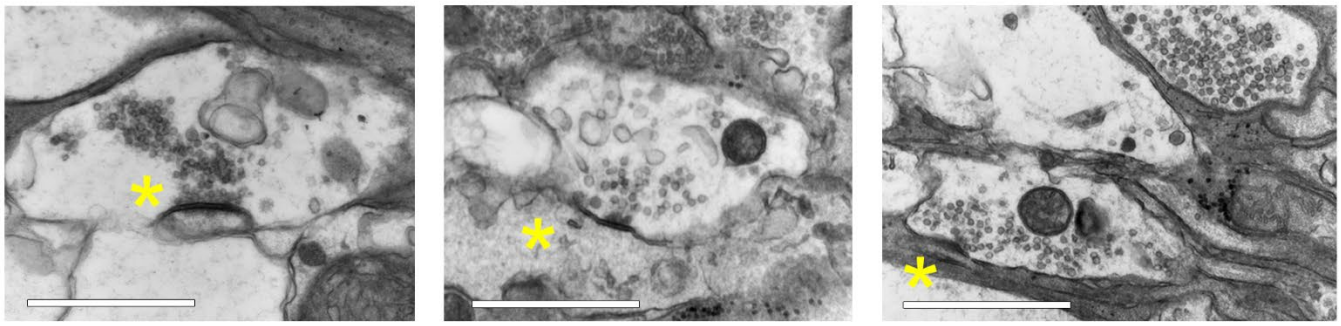

B

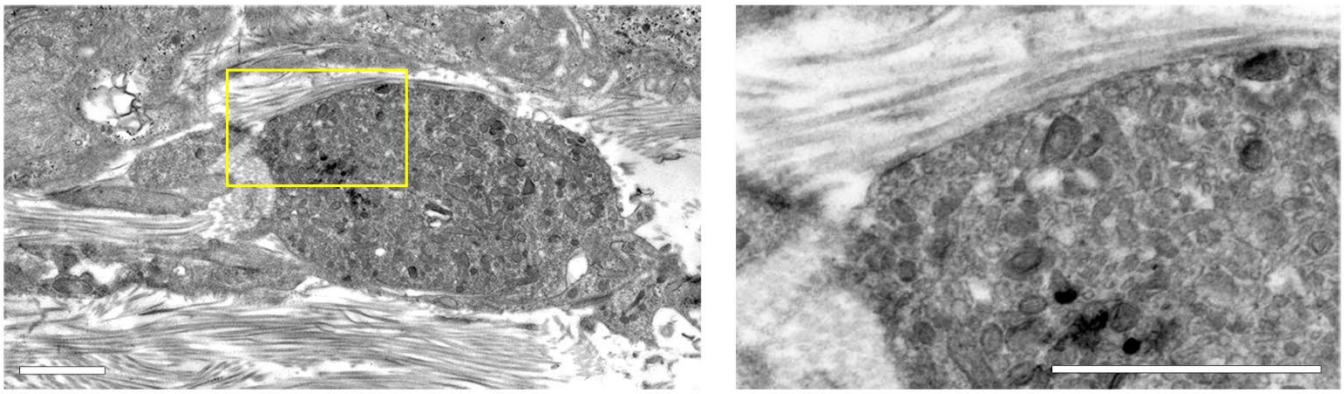

C

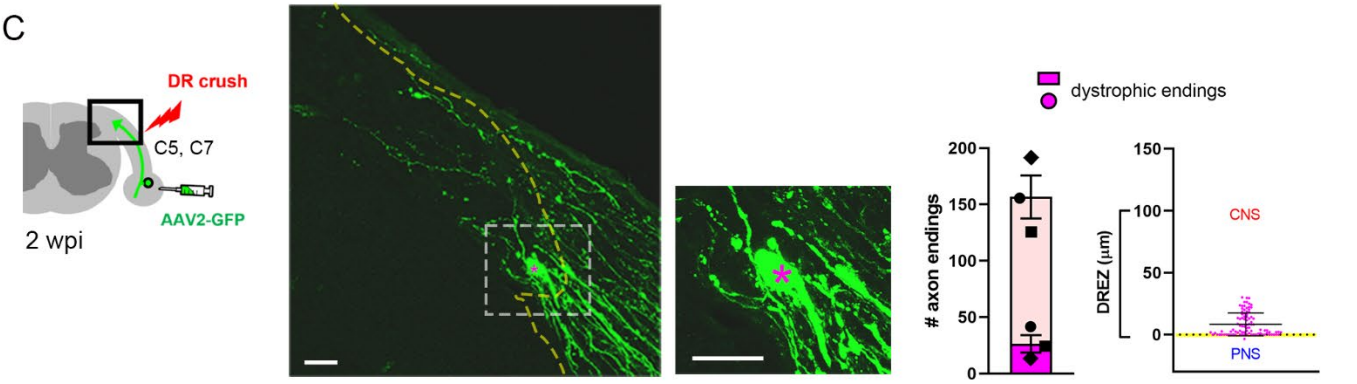


D

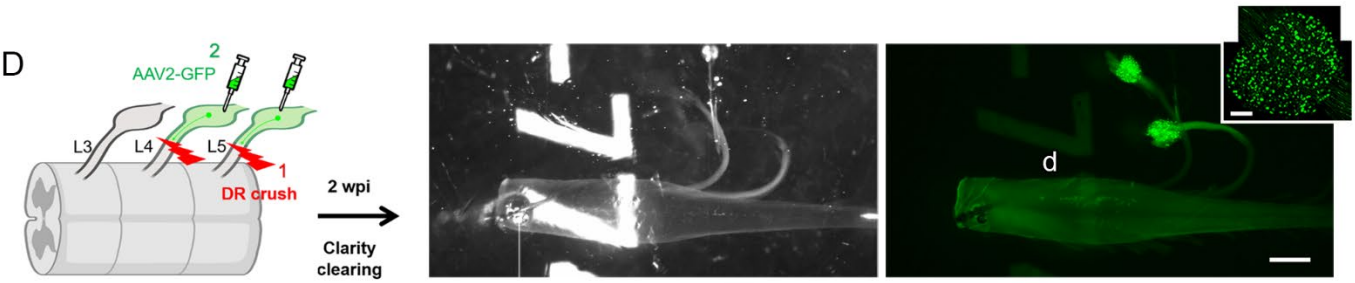


(1) turned-back axons (2) dystrophic endings (3) putative synaptic endings

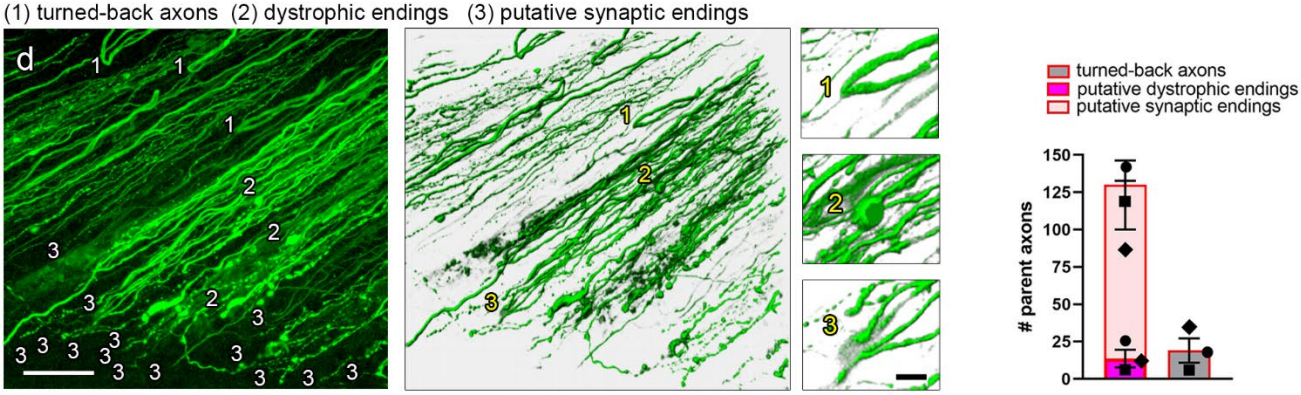

**Figure 1. Dystrophic endings form by axons embedded in collagen fibers at the borderline**

**(A, B)** Ultrastructural comparison of synaptic-like profiles (A) and a dystrophic ending (B) formed by DR axons at the DREZ at 2 wpi. The presynaptic axons exhibiting clustered vesicles are small and opposed to unknown postsynaptic cells exhibiting thin postsynaptic density (asterisks), whereas the dystrophic ending is large, disorganized, and embedded in acellular collagen fibers. Scale bar: 500nm

**(C)** The incidence and location of dystrophic endings analyzed on transverse sections, at 2 weeks after C5-C8 root crush followed by AAV2-GFP injections to C5 and C7 DRGs. A representative section, with enlarged view, showing a large dystrophic ending (asterisk) formed at the borderline (dotted line). Note that many other axons stopped past the borderline do not display dystrophic endings. Graphs show the incidence of dystrophic endings and their location relative to the borderline (n= >100 axons/mouse, 3 mice; putative synaptic endings, 156.7±19.10; dystrophic endings, 26.33±7.688; locations of dystrophic endings (n=91), 8.308±9.233). Error bars represent SD. Scale bar: 20µm

**(D)** High resolution 3D imaging and quantitative analysis of axon endings on wholemounts of CLARITY cleared spinal cords at 2 weeks after L4 and L5 root crush. Transmitted light and fluorescent views of a representative cleared spinal cord, roots, DRG (inset), and GFP+ axons arrested at the DREZ in enlarged (d) or volume rendered images. Representative examples illustrate parental axons that turn around (e.g., 1), form a large dystrophic ending (e.g., 2), or form a small putative synaptic ending (e.g., 3). Relative incidence of different axon endings illustrating that a limited number of parental axons turned around or stopped by forming dystrophic endings. n= >100 axons/mouse, 3 mice. Putative synaptic endings, 116.3±16.33; turned-back axons, 13.67±5.925; dystrophic endings, 19.0±8.185. Error bars represent SD. Scale bars: 200µm (clearing), 50µm (DRG), 50µm (3D, volume), 10µm (enlarged 3D)

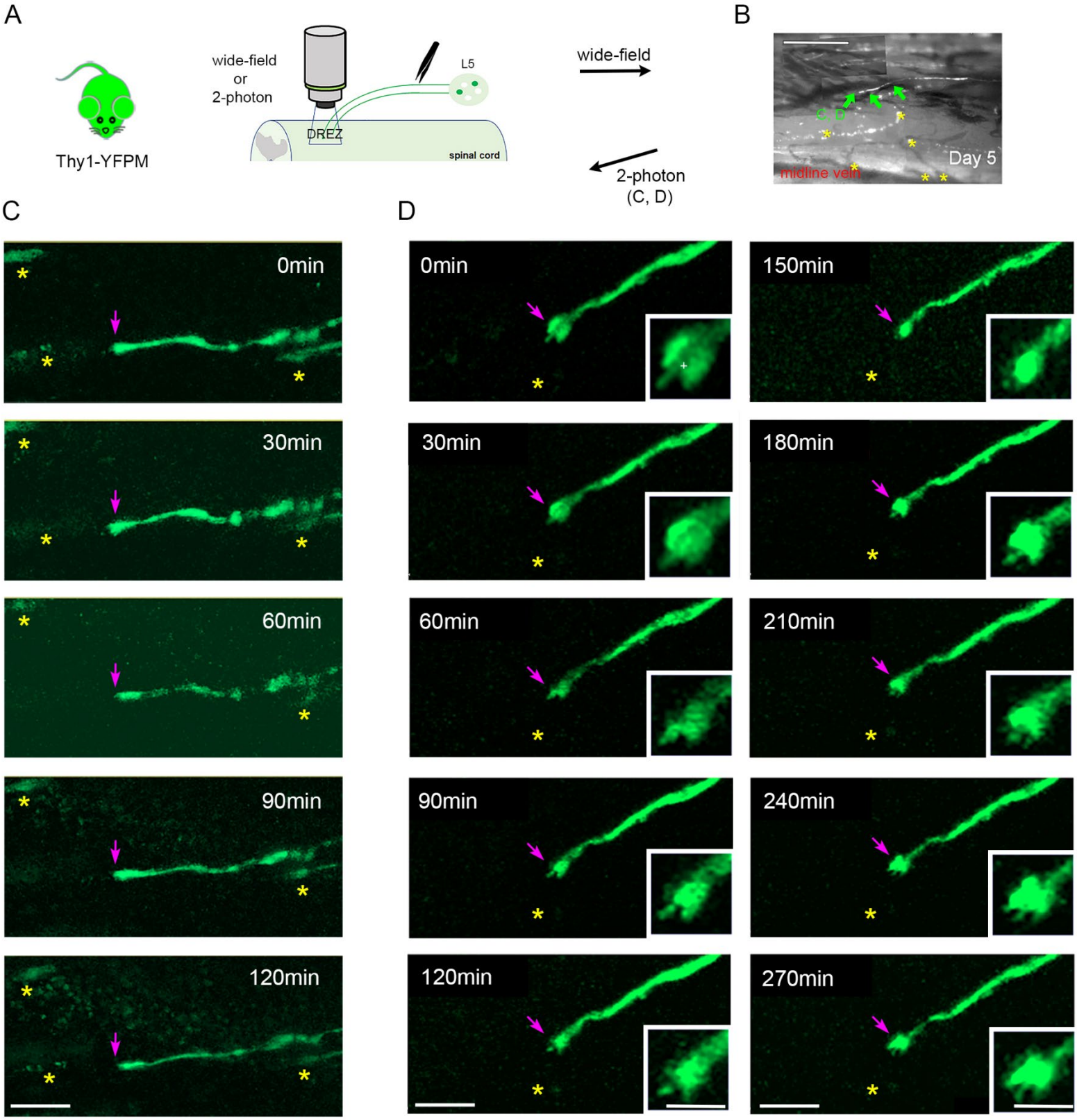


**Figure 2. Two-photon imaging confirms rapid axon immobilization at the DREZ**
**(A)** Schematic illustration of the experimental procedure for two-photon imaging of DR axons in live Thy1-YFPM mice after L5 root crush.
**(B)** A widefield view of the DREZ area, taken at 5 dpi, showing an axon of interest (arrows) and fluorescent debris of degenerating old axons and a midline vein that served as landmarks (asterisks). Scale bar:100µm

**(C, D)** Two-photon imaging of representative axon tips with either slender (C) or small roundish shape (D), taken every 30 min on 5 dpi. Arrows denote immobile axon tips and asterisks denote landmarks. Scale bar: 50μm (C, D), 20μm (D, insets)

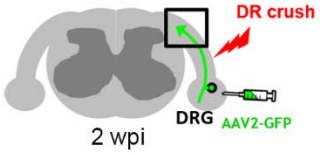
DR crush
DRG
AAV2-GFP
2 wpi

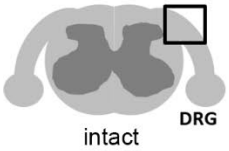
DRG
intact

A

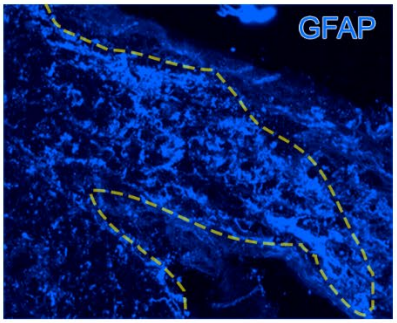
GFAP

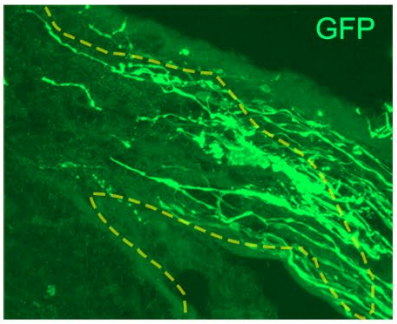
GFP

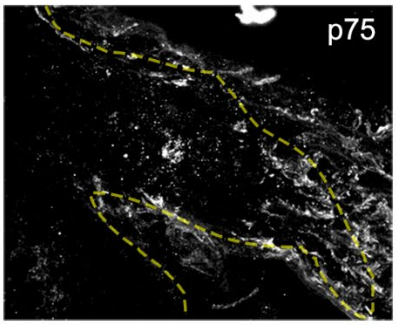
p75

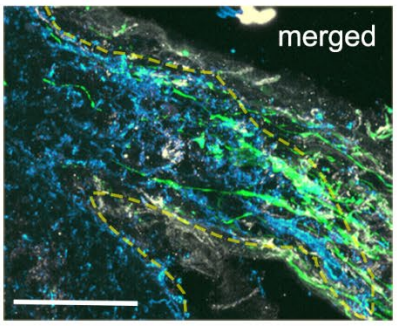
merged

B

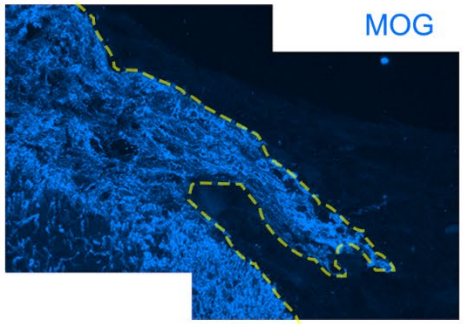
MOG

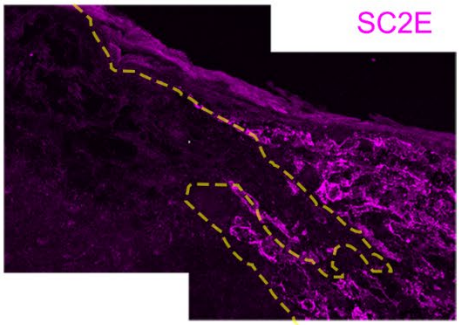
SC2E

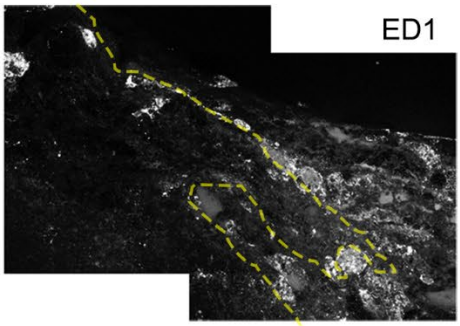
ED1

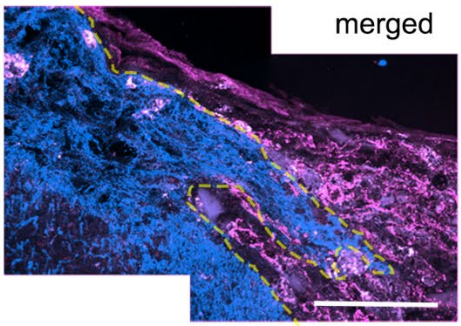
merged

D

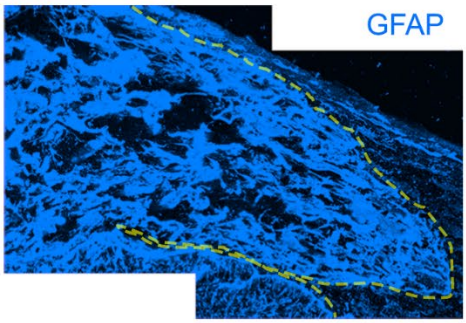
GFAP

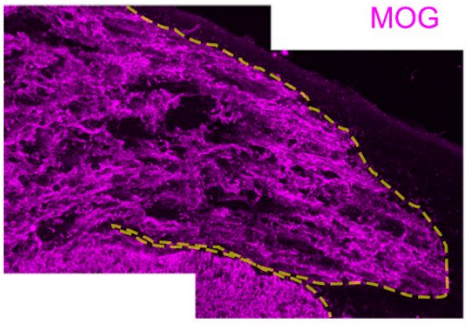
MOG

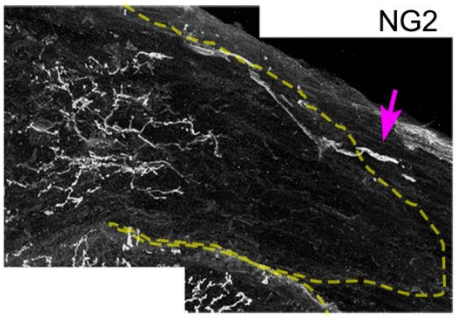
NG2

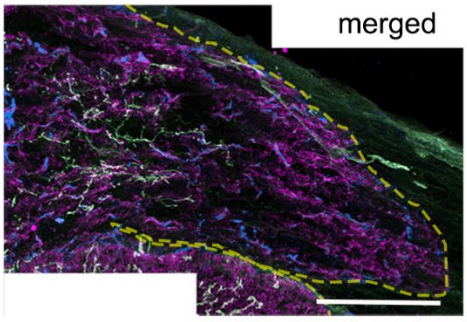
merged

C

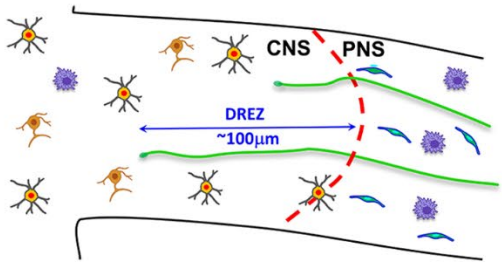
CNS
PNS
DREZ
~100µm

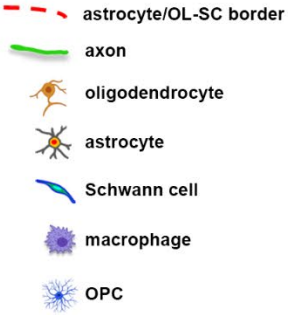
astrocyte/OL-SC border
axon
oligodendrocyte
astrocyte
Schwann cell
macrophage
OPC

E

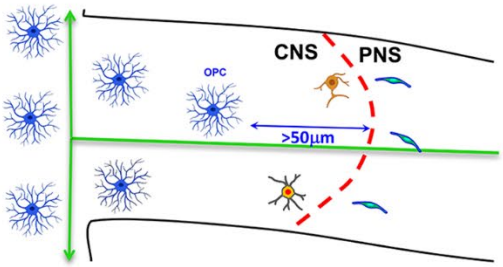
CNS
PNS
OPC
>50µm

**Figure 3. Relative positions of non-neuronal cells and arrested axons at the DREZ**

**(A, B)** Transverse sections of a spinal cord 2 weeks after cervical root crush followed by intraganglionic injection of AAV2-GFP.

**(A)** A DREZ area illustrating spatial relationships of arrested GFP+ axons (Green) with GFAP-labeled astrocytes (Blue) and p75-labeled Schwann cell processes (B/W). Many axons extend across the borderline (dotted line) by growing through astrocytes without association with leading Schwann cell processes. Scale bar: 50μm

**(B)** A DREZ area illustrating spatial relationships of arrested axons (refer to A) with MOG-labeled oligodendrocytes (Blue), SC2E-labeled myelinating Schwann cells (Magenta), and ED1-labeled macrophages (B/W). Macrophages are sparse at the DREZ. Scale bar: 50μm

**(C)** Diagram summarizing insignificant spatial relationships of arrested axons with oligodendrocytes, astrocytes, Schwann cells, and macrophages at axotomized DREZ.

**(D)** A DREZ area of uninjured DRs illustrating that NG2-labeled OPCs (B/W) are absent at and immediately near the borderline (dotted line), denoted by astrocytes (Blue) and oligodendrocytes (Magenta), but abundant deeper at the DREZ (>50μm from the borderline). Arrow denotes NG2+ pericytes associated with a blood vessel. Scale bar: 50μm

**(E)** Diagram illustrating the distance and position of OPC processes relative to the borderline (dotted line) at intact DREZ with no axon injury.

See also **Figure S1 and S2**

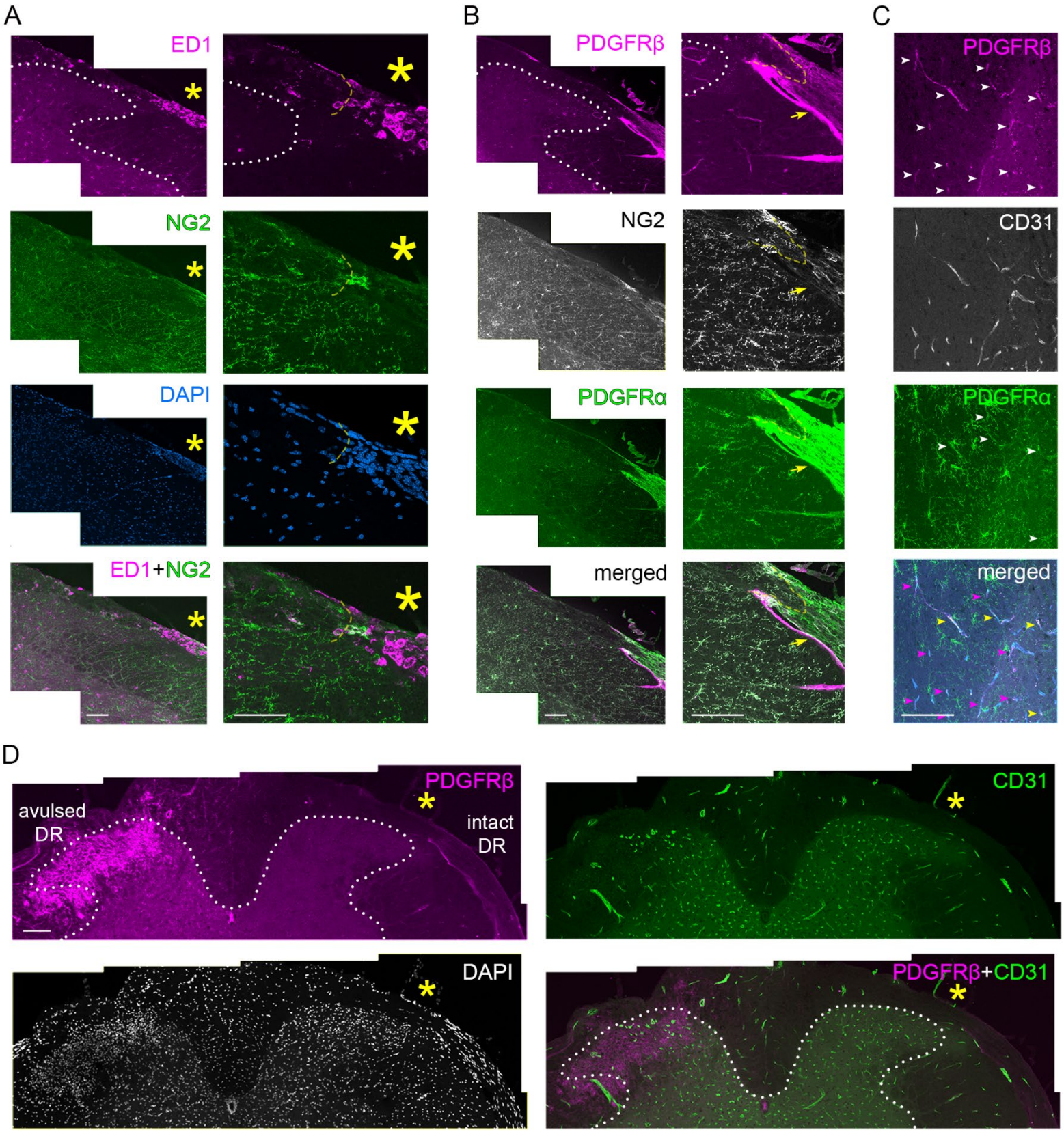


**Figure S1. Macrophages, pericytes, fibroblast-like cells, and blood vessels are sparse at intact and axotomized DREZ**

**(A)** Transverse sections of a spinal cord at 2 wpi, showing low and high magnification views of DREZ area. Asterisks denote numerous macrophages (Magenta) enriched peripherally along the root. Macrophages are

sparse at the DREZ and NG2+ (Green). Yellow dotted line denotes borderline identified by peripherally enriched nuclei. White dotted line denotes grey matter. Scale bar: 100μm

**(B)** Transverse sections of a spinal cord at 2 wpi, showing low and high magnification views of the DREZ area. Pericytes and VLMCs, labeled by PDGFRβ (Magenta), are sparse at the DREZ and appear to be perivascular as indicated by those within the spinal cord. Arrows denote PDGFRβ+/NG2-/PDGFRα+ meningeal fibroblasts associated with the nerve root. NG2 and PDGFRα staining overlaps closely at the DREZ. Because few if any other types of NG2+/PDGFRα+ cells (i.e., VLMCs) are present at the DREZ, almost all NG2+ cells at the DREZ are OPCs and their processes. Scale bar: 100μm

**(C)** Transverse sections of a spinal cord at 2 wpi, showing high magnification views of grey matter. All pericytes and VLMCs, labeled by PDGFRβ (White arrowheads), remain associated with blood vessels (B/W) after DR injury. Some PDGFRβ labeling is not co-localized with PDGFRα staining (Magenta arrowheads), consistent with the notion that VLMCs, but not pericytes, express PDGFRα. Scale bar: 100μm

**(D)** Low magnification views of transverse sections of a spinal cord showing an intact (right) and severely avulsed (left) root. Glial/fibrotic scar was intentionally elicited by severely avulsing C5-C6 roots to damage dorsal spinal cord. The scar is filled with numerous PDGFRβ+ cells. In contrast, PDGFRβ+ cells are sparse at the DREZ (asterisks) and spinal cord with an intact root or after root crush (**B**). Note also that blood vessels (Green) are sparse at the DREZ. Scale bar: 100μm

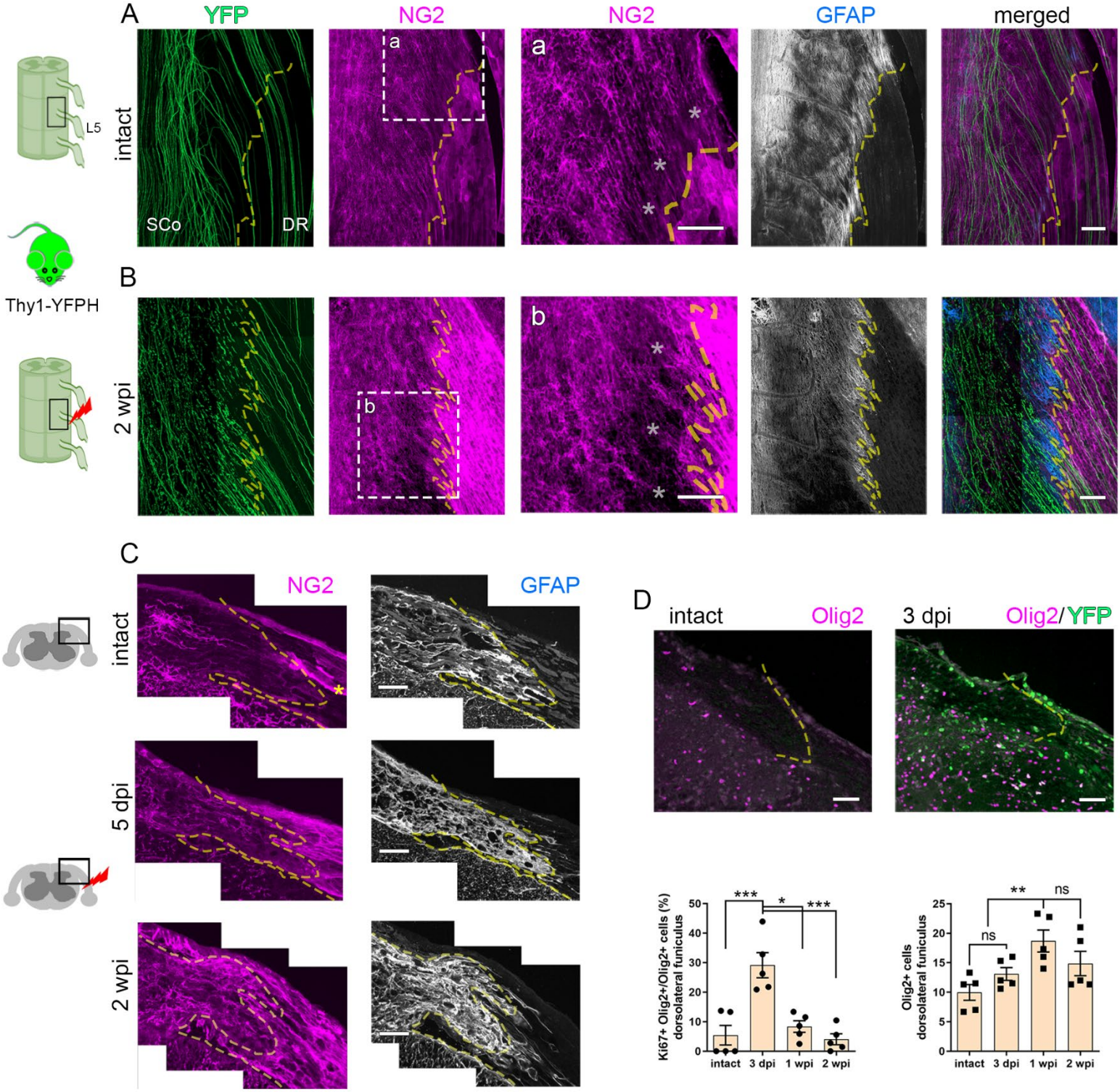


**Figure S2. OPCs proliferate, migrate, and form a dense meshwork of processes after DR injury**
**(A, B)** Wholemount views of intact (A) and axotomized (B) DREZ area showing subsets of YFP+ axons (Green) and the distribution of NG2-labeled OPCs and their processes (Magenta). Dotted line approximates the borderline denoted by GFAP-labeled astrocytes (B/W, Blue). Enlarged images (a, b) show area near the borderline (asterisks) and deeper in CNS territory. Scale bar: 100µm
**(C)** Transverse sections of intact or axotomized DREZ at 5 dpi and 2 wpi, co-labeled for NG2 (Magenta) and GFAP (B/W, Blue), illustrating temporal development of a dense meshwork of OPC processes populating the DREZ after DR injury. Asterisk denotes NG2-labeled blood vessels. Scale bar: 50µm

**(D)** Quantification of OPC proliferation by counting nuclei co-labeled by Olig2, a marker of OPCs and oligodendrocytes, and Ki67, a marker of cell proliferation. N= >3 sections/each mouse, 5 mice/each time point. Ki67+Olig2+: intact, 5.405±3.310; 3 dpi, 29.23±4.260; 1 wpi, 8.359±1.945; 2 wpi. 4.047±1.845. Olig2+: intact, 9.967±1.327; 3 dpi, 13.09±1.082; 1 wpi, 18.68±1.859; 2 wpi 14.87±2.065. Error bars represent SEM. p values are calculated by one-way repeated measures ANOVA with Tukey's post hoc test. ns, $p > 0.05$; *$p \leq 0.01$, **$p \leq 0.001$, ***$p \leq 0.0001$.

**(D)** Quantification of OPC proliferation by counting nuclei colabeled by Olig2, a marker of OPCs and oligodendrocytes (D1), and Ki67, a marker of cell proliferation (D2), illustrating rapid proliferation of OPCs after DR injury that peaks at 3 dpi (D3) and doubles the number of Olig2+ cells by 1 wpi (D4). N= >3 sections/each mouse, 5 mice/each time point. Error bars represent SEM. p values are calculated by one-way repeated measures ANOVA with Tukey's post hoc test. ns, $p > 0.05$; *$p \leq 0.01$, **$p \leq 0.001$, ***$p \leq 0.0001$.

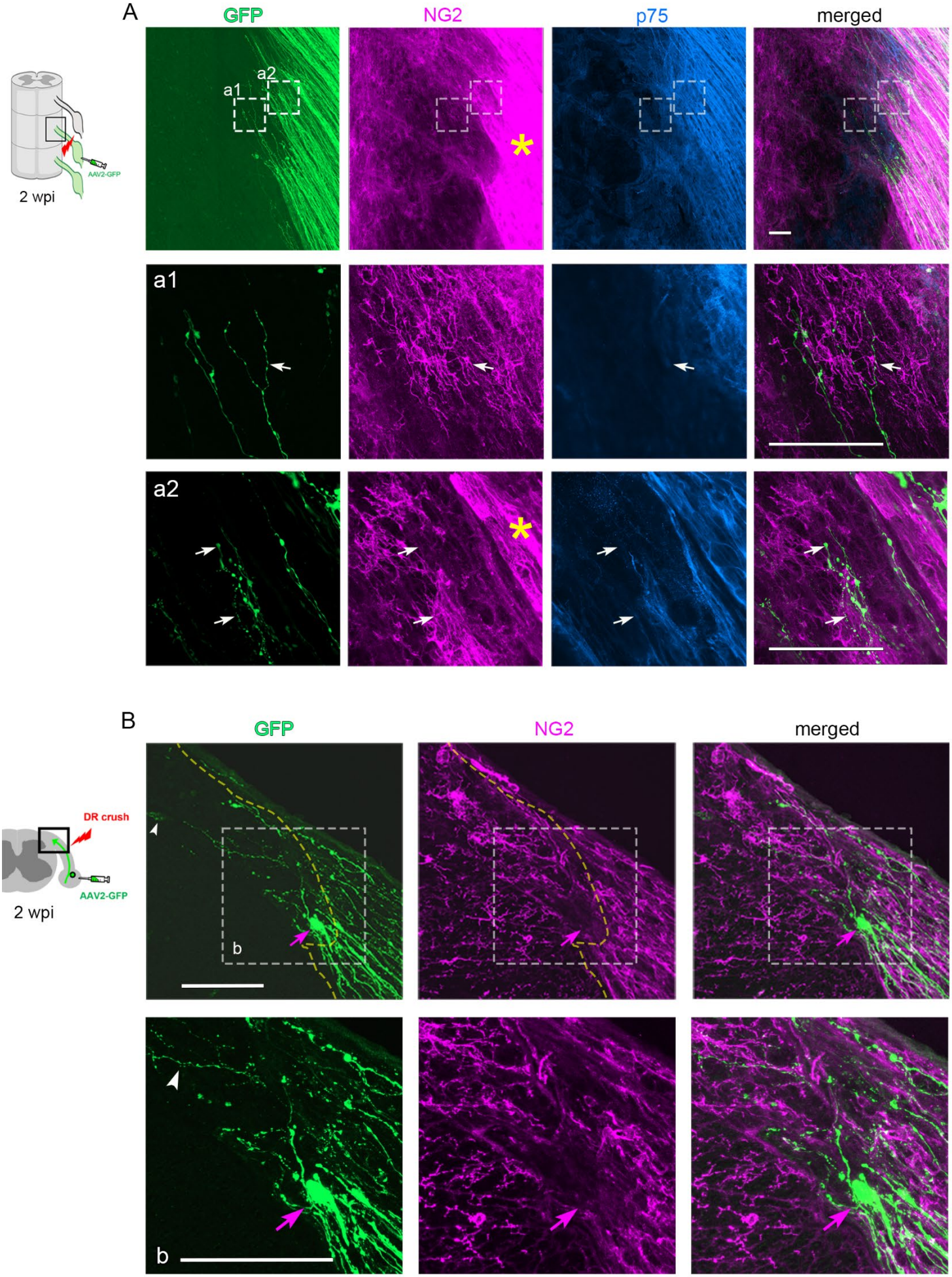
A
GFP
NG2
p75
merged
a1
a2
AAV2-GFP
2 wpi
B
DR crush
AAV2-GFP
2 wpi
b

**Figure 4. Stopped axons without dystrophic endings display extensive contacts with OPC processes**
**(A)** Wholemount views of the DREZ area in low and high magnifications at 2 wpi, showing GFP+ axons (Green), NG2-labeled OPCs (Magenta), and p75-labeled Schwann cells (Blue). Arrows indicate examples of direct contacts between OPC processes and arrested axons. NG2 staining in the PNS (asterisks) is intense after DR injury but does not preclude identification of OPC processes. Scale bar: 100µm
**(B)** Transverse sections in low and high (b) magnifications showing GFP+ axons (Green) and NG2-labeled OPCs (Magenta) at 2 wpi. Arrowheads indicate an example of many axons that stopped past the borderline (dotted line) in association with OPC processes. Arrows indicate a dystrophic ending formed at the borderline that, in contrast, lacks contacts with OPC processes. Scale bar: 50µm

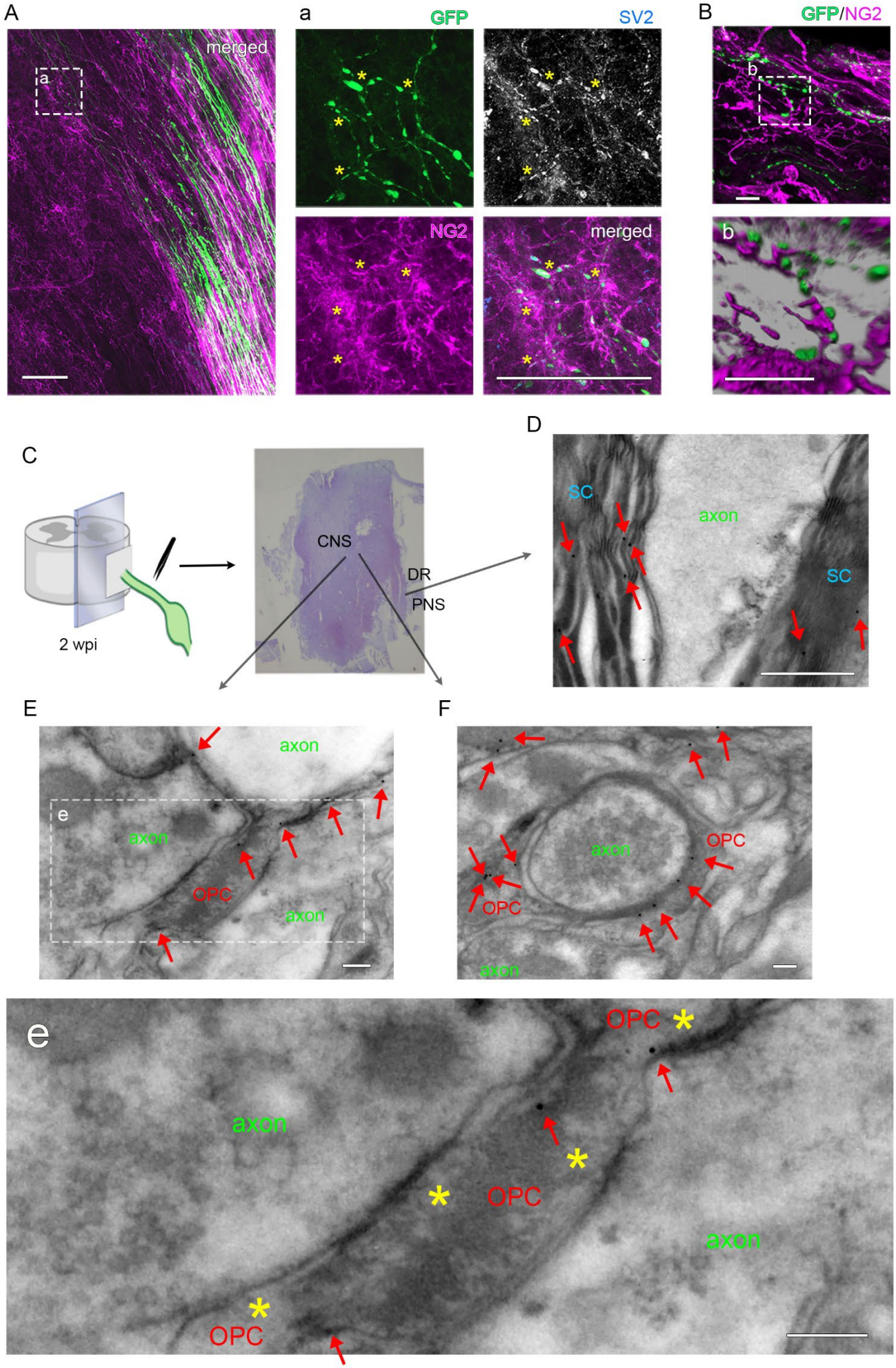
A
merged
a
a
GFP
SV2
NG2
merged
B
GFP/NG2
b
b
C
2 wpi
CNS
DR
PNS
D
SC
axon
SC
E
axon
e
axon
OPC
axon
F
axon
OPC
OPC
axon
e
OPC
axon
OPC
axon
OPC

**Figure 5. DR axons arrested at the DREZ form synapses with OPC processes**

**(A)** Wholemount views of the DREZ area at 2 wpi in low and high magnifications (a), showing GFP-labeled axons (Green), SV2-labeled synaptic vesicles (B/W), and NG2-labeled OPCs (Magenta). Boxed area shows several axons with small swellings on axon tips and shafts intensely labeled for SV2 and tightly associated with OPC processes. Asterisks indicate same positions. Scale bar: 100μm (A), 50μm (a)

**(B)** Volume rendered image (b) of a boxed area in B, illustrating direct contacts of axon swellings (Green) with OPC processes (Magenta). Scale bar: 5μm

**(C)** Diagram showing procedures to prepare a longitudinal vibratome slice of dorsal spinal cord with attached DR at 2 wpi.

**(D)** An electron micrograph of the PNS area showing gold particles (arrows) targeted to NG2 selectively labeling Schwann cells (SC). Scale bar: 500 nm

**(E)** An area of the DREZ showing that OPC processes denoted by gold particles (arrows) form synaptic contacts with axons. Magnified view of boxed area (e) illustrates synaptic profiles (asterisks) with presynaptic clustering of synaptic vesicles and postsynaptic density. Scale bar: 100 nm

**(F)** An electron micrograph illustrating varicosity-like synaptic profile formed by DR axon encircled by OPC processes identified by gold particles (arrows). Scale bar: 100 nm

See also **Figure S3**

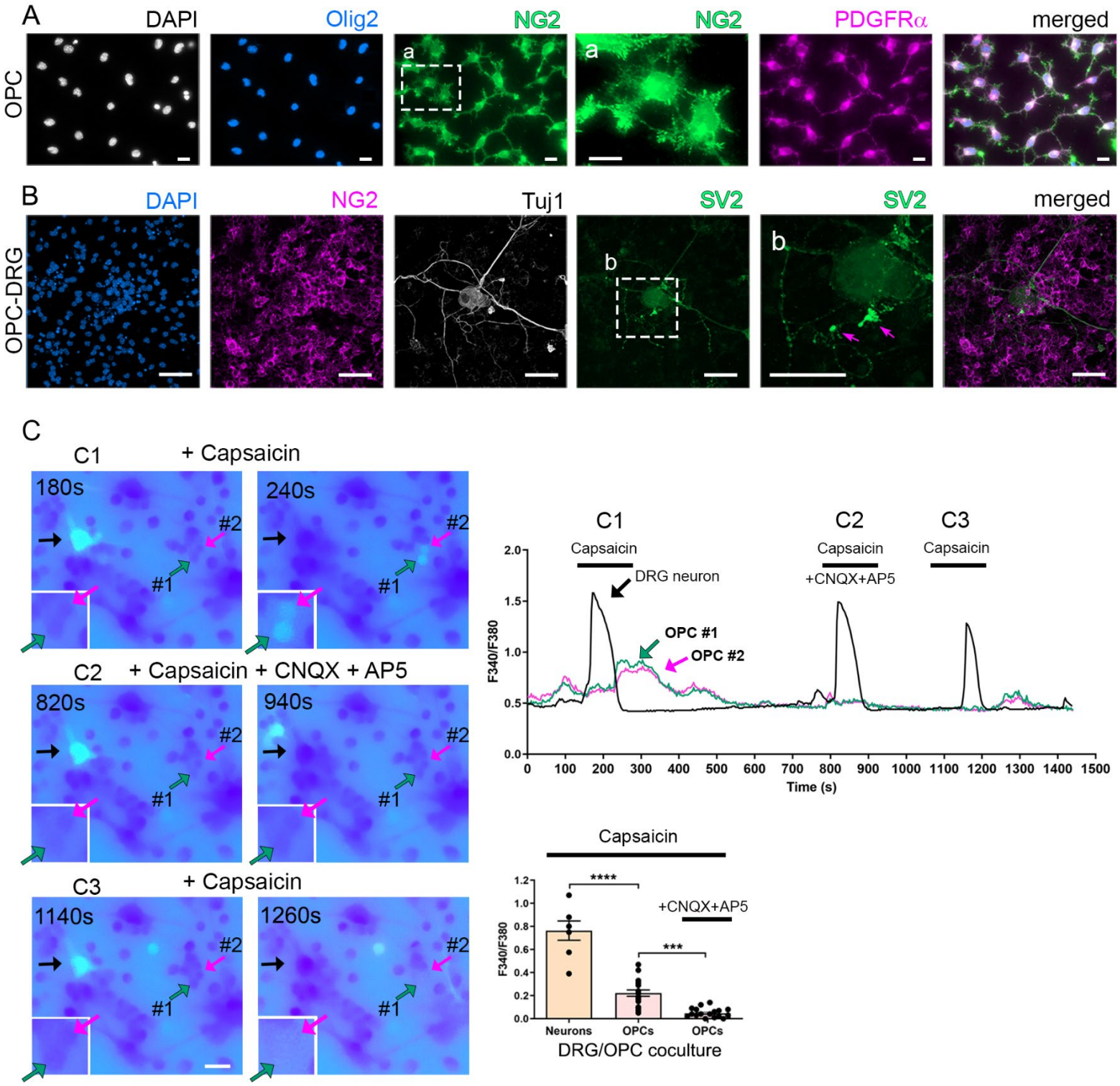


**Figure S3. OPCs form functional synapses with co-cultured DRG neurons**

**(A)** >95% pure OPCs, cultured from spinal cords of p16-18 mice, immunolabeled at 3 div for DAPI, Olig2, NG2 and PDGFRα. Enlarged view (a) of boxed area illustrates OPCs with bushy processes resembling OPCs *in vivo*. Scale bar: 20µm

**(B)** Purified OPCs and DRG neurons co-cultured for 5 days, showing DAPI, NG2-labeled OPCs, Tuj1-labeled axons, and SV2-labeled synaptic vesicles. Magnified view (b) of boxed area illustrates microtubule-deficient but SV2-enriched axonal swellings (arrows) formed on OPCs. Scale bar: 50µm

**(C)** Representative calcium imaging recordings of OPC-DRG neurons co-cultured for 5 days, illustrating temporal calcium responses of a neuron (Black arrows) and two adjacent OPCs (Green and Magenta arrows), following capsaicin stimulation of neurons without (C1) or with antagonists of AMPA/kainate and NMDA receptors (C2), CNQX and AP5. Following washout of antagonists (C3), capsaicin stimulation of the same neuron again elicits calcium responses in the same OPCs. Graph shows comparisons of capsaicin-elicited calcium responses in DRG neurons and OPCs. n = 7-18. Neurons, 0.76±0.05; OPCs, 0.22±0.06; OPCs, 0.05± 0.04. Error bars represent SEM. p values are calculated by one-way repeated measures ANOVA with Tukey's post hoc test. ***$p \leq 0.001$, ****$p \leq 0.0001$. Scale bar: 30µm

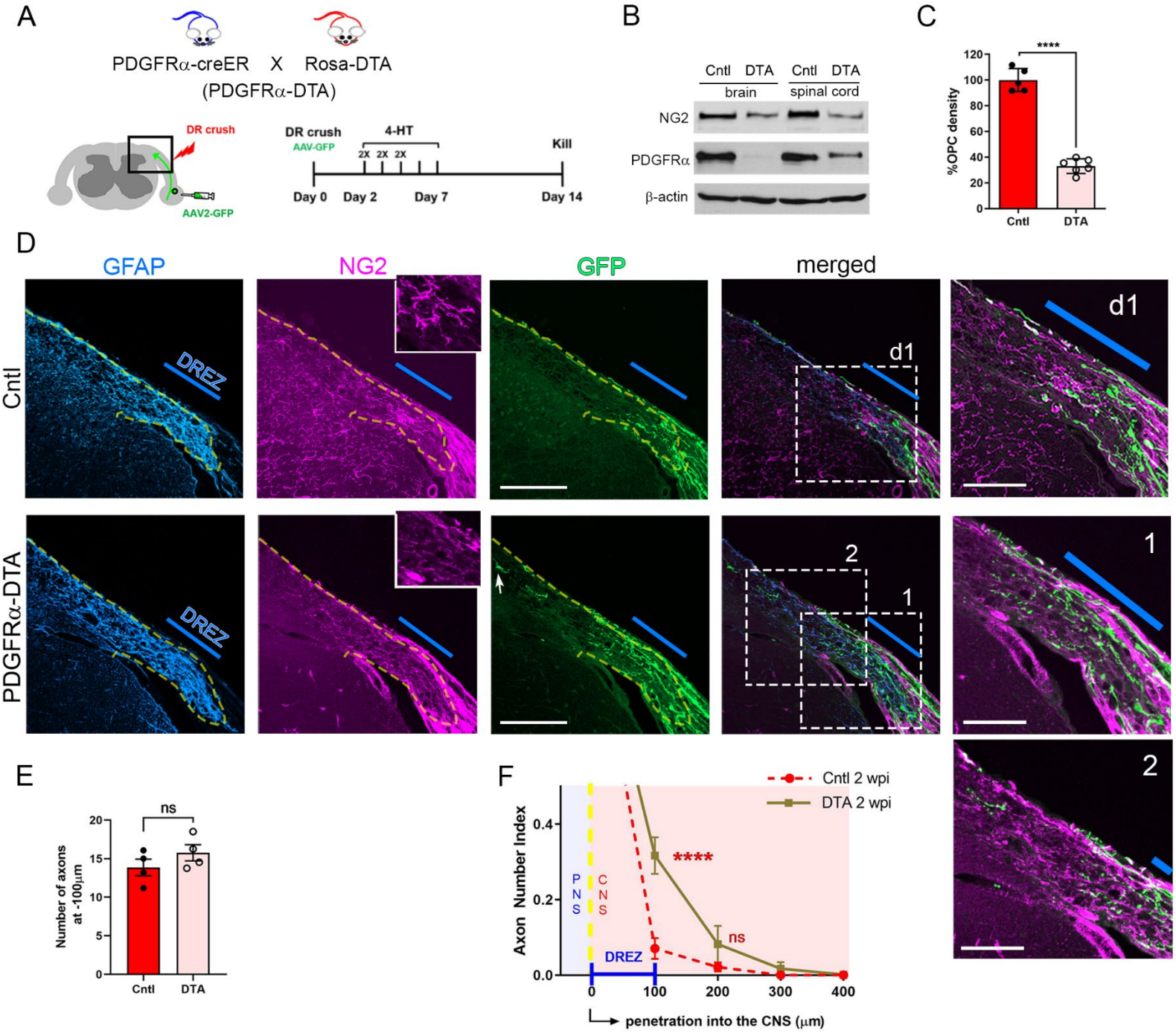


**Figure 6. Genetic OPC ablation, although incomplete, markedly enhances regeneration across the DREZ**
**(A)** Diagram illustrating experimental procedures to evaluate the effects of genetic OPC ablation at 2 weeks after C5-C8 root crush followed by AAV2-GFP injections to C5 and C7 DRGs.
**(B)** Western blotting showing markedly reduced markers of OPCs, NG2, and PDGFRα, in PDGFRα-DTA mice.
**(C)** Quantitative comparisons of OPC density measured by mean fluorescence intensity of NG2 staining in the spinal cord, illustrating ~70% ablation of OPCs in PDGFRα-DTA mice used for the analysis. Cntl, 100.0±8.992; DTA, 33.07±5.725. Error bars represent SD. Unpaired t test (n=5 control, 6 DTA mice). ****$p \leq 0.00001$
**(D)** Transverse sections of a control and a PDGFRα-DTA mouse with ~80% OPC ablation at 2 wpi showing GFAP-labeled astrocytes (Blue), NG2-labeled OPCs (Magenta), and GFP+ axons (Green). Enlarged views of

boxed area (d1, 1, 2) illustrate that more axons cross the border and DREZ in the PDGFRα-DTA mouse. Blue lines approximate ~100μm wide region of the DREZ. Dotted lines denote borderline identified by GFAP staining. Insets are magnified views of the DREZ, illustrating residual and/or repopulating OPCs in PDGFRα-DTA mice. An arrow denotes axons extending unusually deeply into the dorsal funiculus. Scale bar: 100μm, 50μm (insets)

**(E)** Quantification of GFP+ axons at ~100μm proximal to the borderline in the PNS. Cntl, 13.86±1.075; DTA, 15.76±1.052. Error bars represent SEM (n = 4 mice/group). Unpaired Student's t-test. ns, $p > 0.05$

**(F)** Quantitative comparisons of control and PDGFRα-DTA mice illustrating that OPC ablation triples the number of axons extending past the DREZ. Cntl: 0μm, 1.00±0; 100μm, 0.0765±0.02744; 200μm, 0.02128±0.01181; 300μm, 0.00±0.00. DTA: 0μm, 1.00±0.00; 100μm, 0.3167±0.0485; 200μm, 0.08238±0.04858; 300μm, 0.01723±0.01723; 400μm, 0.001375±0.001375. Error bars represent SEM (n=4 mice/group). Two-way repeated-measures ANOVA with Tukey's multiple comparisons test. 100μm, ****$p \leq 0.00001$; 200μm, ns, $p > 0.05$; 300μm

See also **Figure S4, S5, S6**

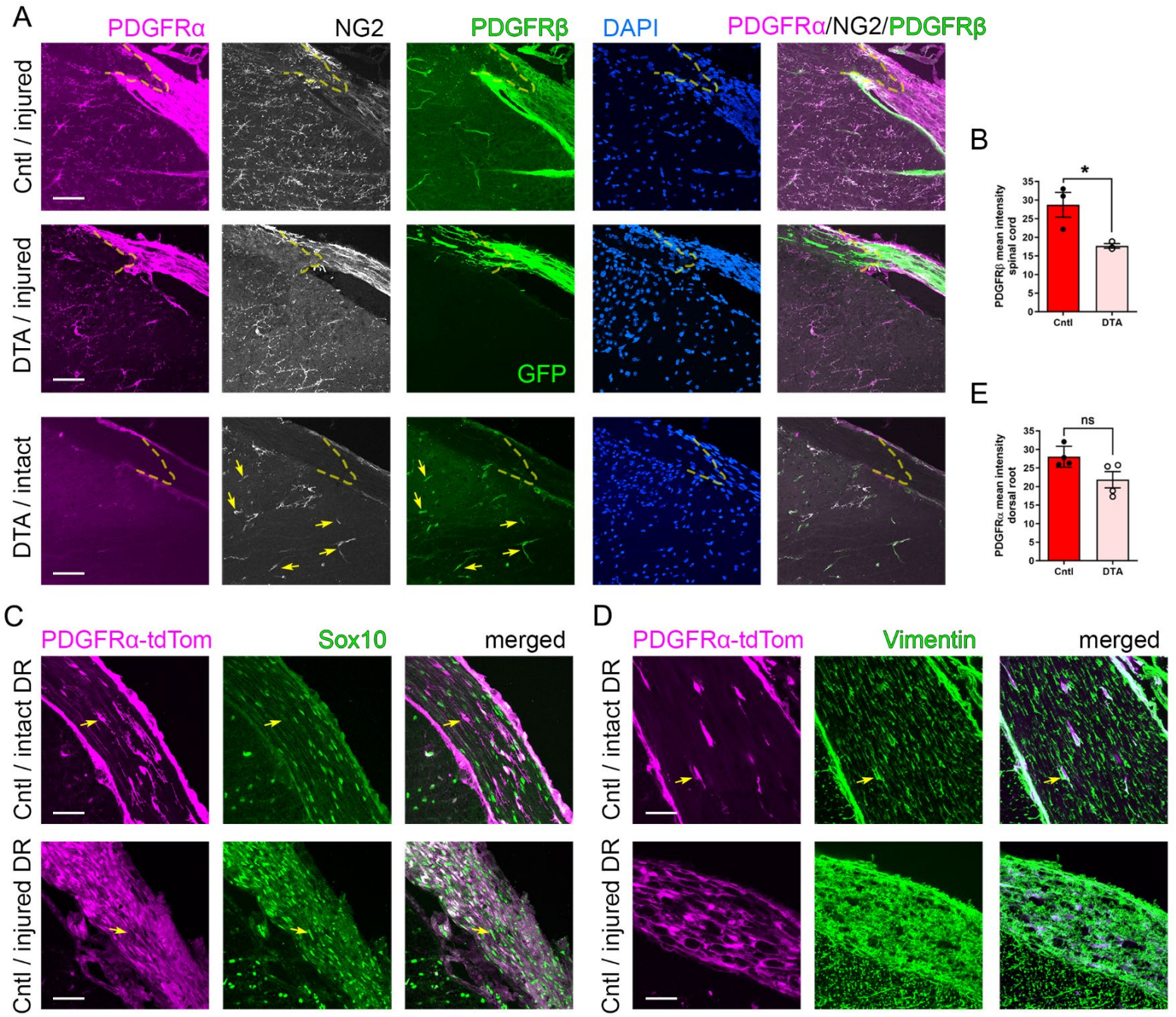


**Figure S4**. **Pericytes and ablation of PGFRα+ cells in PDGFRα-DTA mice**

**(A)** Representative high magnification views of the DREZ area in a control and two PDGFRα-DTA mice, co-labeled for PDGFRα, NG2, and PDGFRβ. A PDGFRα-DTA mouse with ~40% OPC ablation at 2 wpi shows PDGFRα staining closely overlapped with NG2 staining, illustrating ablation of PDGFRα+ cells. Bottom panels show the DREZ area of an uninjured PDGFRα-DTA mouse with ~80% OPC ablation, illustrating unaffected pericytes. NG2+/PDGFRβ+ cells with perivascular morphology (i.e., pericytes; arrows) remain intact, despite almost complete ablation of PDGFRα+ cells in the DREZ area of the DTA mouse. Scale bar: 50μm

**(B)** Quantitative comparisons of control and PDGFRβ-DTA mice, illustrating a reduction of PDGFRβ immunoreactivity in the spinal cord of DTA mice. Quantification of the DREZ area is not provided due to

paucity of PDGFRβ+ cells at the DREZ in both control and DTA mice. Cntl, 28.74±3.344; DTA, 17.69±0.6118**.** Unpaired Student t-test (n=3 control, 3 DTA mice). Error bars represent SEM. *$p \leq 0.01$.

**(C)** High magnification views of dorsal roots of a PDGFRα-tdTomato mouse, showing that PDGFRα+ cells are sparse in an intact dorsal root but abundant in a crushed root at 2 wpi. PDGFRα+ cells are not labeled by Sox10 (arrows), indicating that they are not Schwann cells. Scale bar: 50μm

**(D)** High magnification views of intact and crushed dorsal roots of a PDGFRα-tdTomato mouse, showing that PDGFRα+ cells are co-labeled by a fibroblast marker, vimentin (arrows). Scale bar: 50μm

**(E)** Quantitative comparisons of control and PDGFRα-DTA mice, illustrating insignificant difference in PDGFRα immunoreactivity in the dorsal root. Cntl, 28.04±1.406; DTA. 21.83±2.197. Unpaired Student t-test (n=4 mice/group). Error bars represent SEM. ns, $p > 0.05$

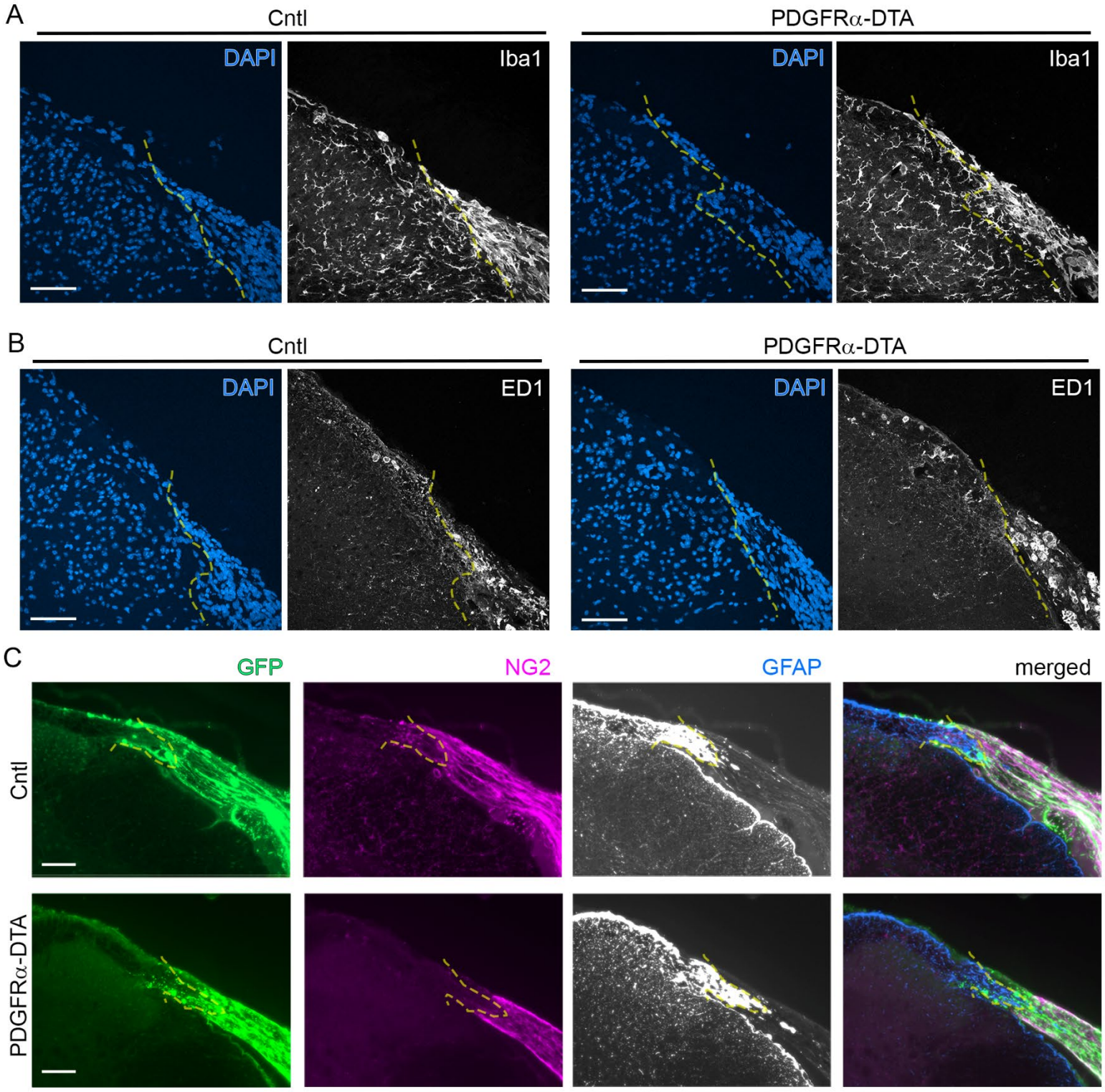
A
Cntl
PDGFRα-DTA
DAPI
Iba1
DAPI
Iba1
B
Cntl
PDGFRα-DTA
DAPI
ED1
DAPI
ED1
C
GFP
NG2
GFAP
merged
Cntl
PDGFRα-DTA

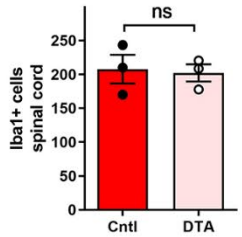
D
ns
Iba1+ cells spinal cord
250
200
150
100
50
0
Cntl
DTA

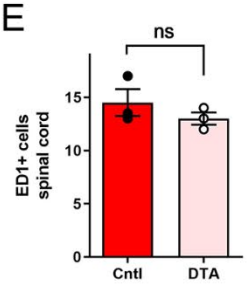
E
ns
ED1+ cells spinal cord
15
10
5
0
Cntl
DTA

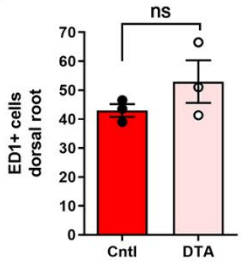
F
ns
ED1+ cells dorsal root
70
60
50
40
30
20
10
0
Cntl
DTA

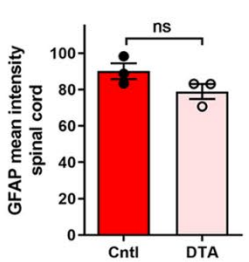
G
ns
GFAP mean intensity spinal cord
100
80
60
40
20
0
Cntl
DTA

**Figure S5**. **Microglia, macrophages and astrocytes in PDGFRα-DTA mice**

**(A)** Transverse sections of a control and a PDGFRα-DTA mouse at 2 wpi, showing DAPI and Iba1-labeled microglia, and illustrating no noticeable differences in morphology or density of microglia in the spinal cord, DREZ, or DR of control and DTA mice. Scale bar: 100μm

**(B)** Transverse sections from a control and PDGFRα-DTA mouse at 2 wpi, showing DAPI and ED1-labeled macrophages, and illustrating no noticeable differences in the distribution or density of macrophages in the spinal cord, DREZ, or DR of control and DTA mice. Scale bar: 100μm

**(C)** Transverse sections of control and PDGFRα-DTA mice at 2 wpi, co-labeled for NG2 and GFAP, illustrating no noticeable differences in the density or distribution of astrocytes at the DREZ or within the spinal cord between control and DTA mice. Scale bar: 50μm

**(D)** Quantitative comparisons of control and PDGFRα-DTA mice illustrating insignificant difference in the number of Iba1+ microglia in the spinal cord. Cntl, 207.8±21.20; DTA, 202.1±12.70. Unpaired Student's t-test (n=3 mice/group). Error bars represent SEM. ns, $p > 0.05$

**(E, F)** Quantitative comparisons of control and PDGFRα-DTA mice, illustrating insignificant difference in the number of ED1+ macrophages in the spinal cord (E) or dorsal root (F). (E) Cntl, 14.50±1.258; DTA, 13.00±0.5774. (F) Cntl, 43.00±2.179; DTA, 52.94±7.330. Unpaired Student's t-test (n=3 mice/group). Error bars represent SEM. ns, $p > 0.05$

**(G)** Quantitative comparisons of control and PDGFRα-DTA mice, illustrating insignificant difference in GFAP immunoreactivity in the spinal cord. Cntl, 90.10±4.363; DTA, 78.95±4.127. Unpaired Student's t-test (n=3 mice/group). Error bars represent SEM. ns, $p > 0.05$

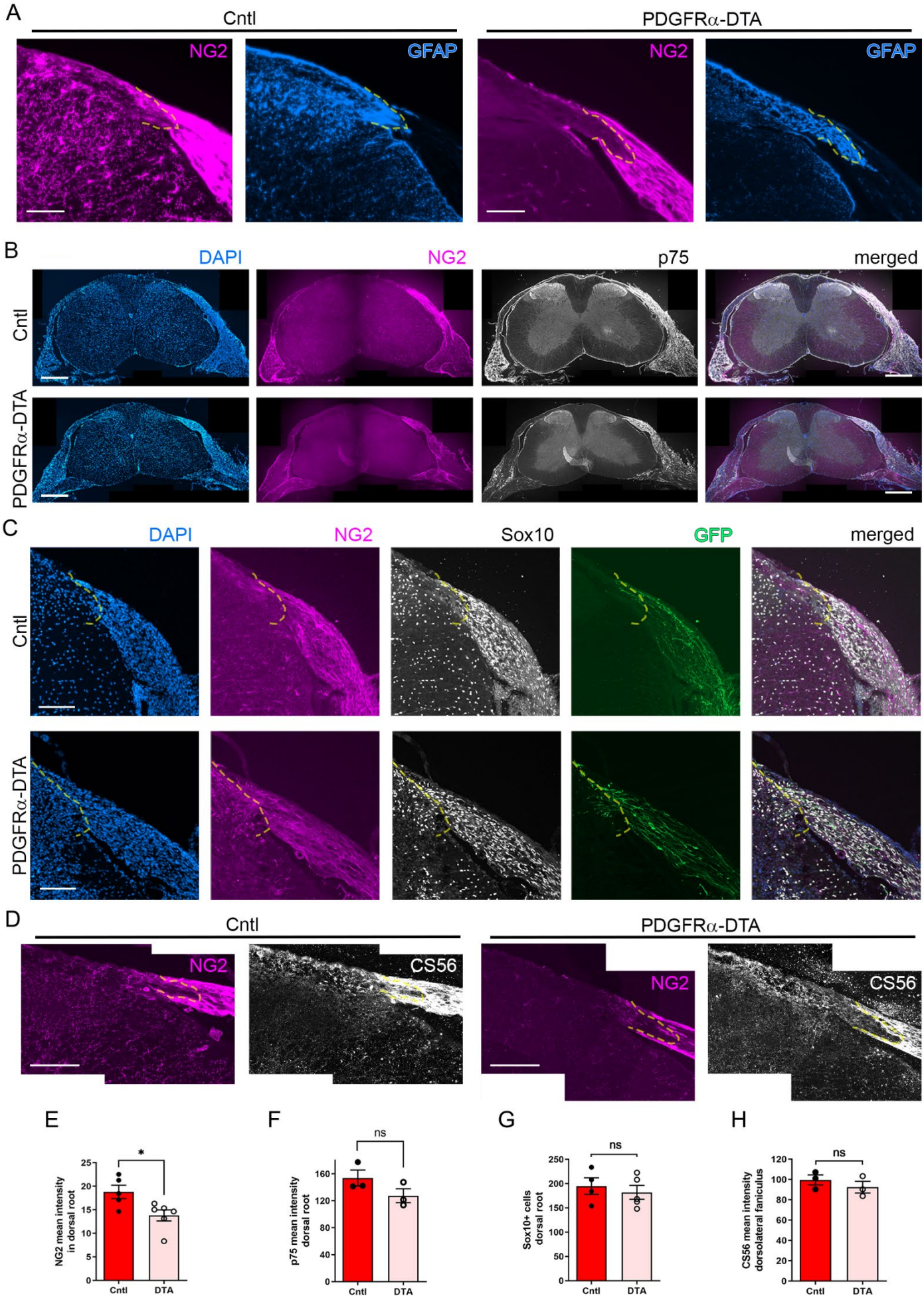
A
Cntl
PDGFRα-DTA
NG2
GFAP
NG2
GFAP
B
DAPI
NG2
p75
merged
Cntl
PDGFRα-DTA
C
DAPI
NG2
Sox10
GFP
merged
Cntl
PDGFRα-DTA
D
Cntl
PDGFRα-DTA
NG2
CS56
NG2
CS56
E
NG2 mean intensity in dorsal root
*
Cntl
DTA
F
p75 mean intensity dorsal root
ns
Cntl
DTA
G
Sox10+ cells dorsal root
ns
Cntl
DTA
H
CS56 mean intensity dorsolateral fanicullus
ns
Cntl
DTA

**Figure S6**. **NG2/CSPG4, Schwann cells and CSPGs in PDGFRα-DTA mice**

**(A)** Transverse sections of a control and a PDGFRα-DTA mouse with ~80% OPCs ablated at 2 wpi, co-labeled for NG2 and GFAP, illustrating a marked reduction in OPCs and their processes in PDGFRα-DTA mouse. NG2 staining is slightly reduced peripherally along the DR of the PDGFRα-DTA mouse, as compared to control mouse. Scale bar: 100μm

**(B)** Transverse sections of control and PDGFRα-DTA mice at 2 wpi, illustrating that p75 immunoreactivity in dorsal root of DTA mouse is comparable to that of control mouse. Scale bar: 500μm

**(C)** Transverse sections of control and PDGFRα-DTA mice at 2 wpi, illustrating no noticeable difference in the number of Sox10-labeled Schwann cells present in the dorsal root. Scale bar: 100μm

**(D)** Transverse sections of a control and a PDGFRα-DTA mouse, co-labeled for NG2 and for CS56 at 2 wpi, showing reduced NG2 but abundant CSPGs associated with the DREZ area of DTA mice. Scale bar: 100μm

**(E)** Quantitative comparisons of control and PDGFRα-DTA mice, illustrating a slight reduction of NG2 immunoreactivity in dorsal roots of DTA mice. Cntl, 18.81±1.419; DTA, 13.81±1.173. Unpaired Student's-t test (n=5 control, 6 DTA mice). Error bars represent SEM. $*p \leq 0.01$

**(F)** Quantitative comparison of control and PDGFRα-DTA mice, illustrating insignificant difference in p75 immunoreactivity in the dorsal root. Cntl, 153.7±11.83; DTA, 117.5±18.55. Unpaired Student's t-test (n=3 mice/group). Error bars represent SEM. ns, $p > 0.05$

**(G)** Quantitative comparison of control and PDGFRα-DTA mice, illustrating insignificant difference in the number of Schwann cells in the dorsal root. Cntl, 195.0±17.03; DTA 182.1±14.19. Unpaired Student's t-test (n= 4 control, 5 DTA mice). Error bars represent SEM. ns, $p > 0.05$

**(H)** Quantitative comparisons of control and PDGFRα-DTA mice, illustrating insignificant difference in CS56 immunoreactivity measured in the dorsolateral funiculus including the DREZ. Cntl, 99.58.0±4.926; DTA 92.46±5.748. Unpaired Student's t-test (n=3 control, 3 DTA mice). Error bars represent SEM. ns, $p > 0.05$

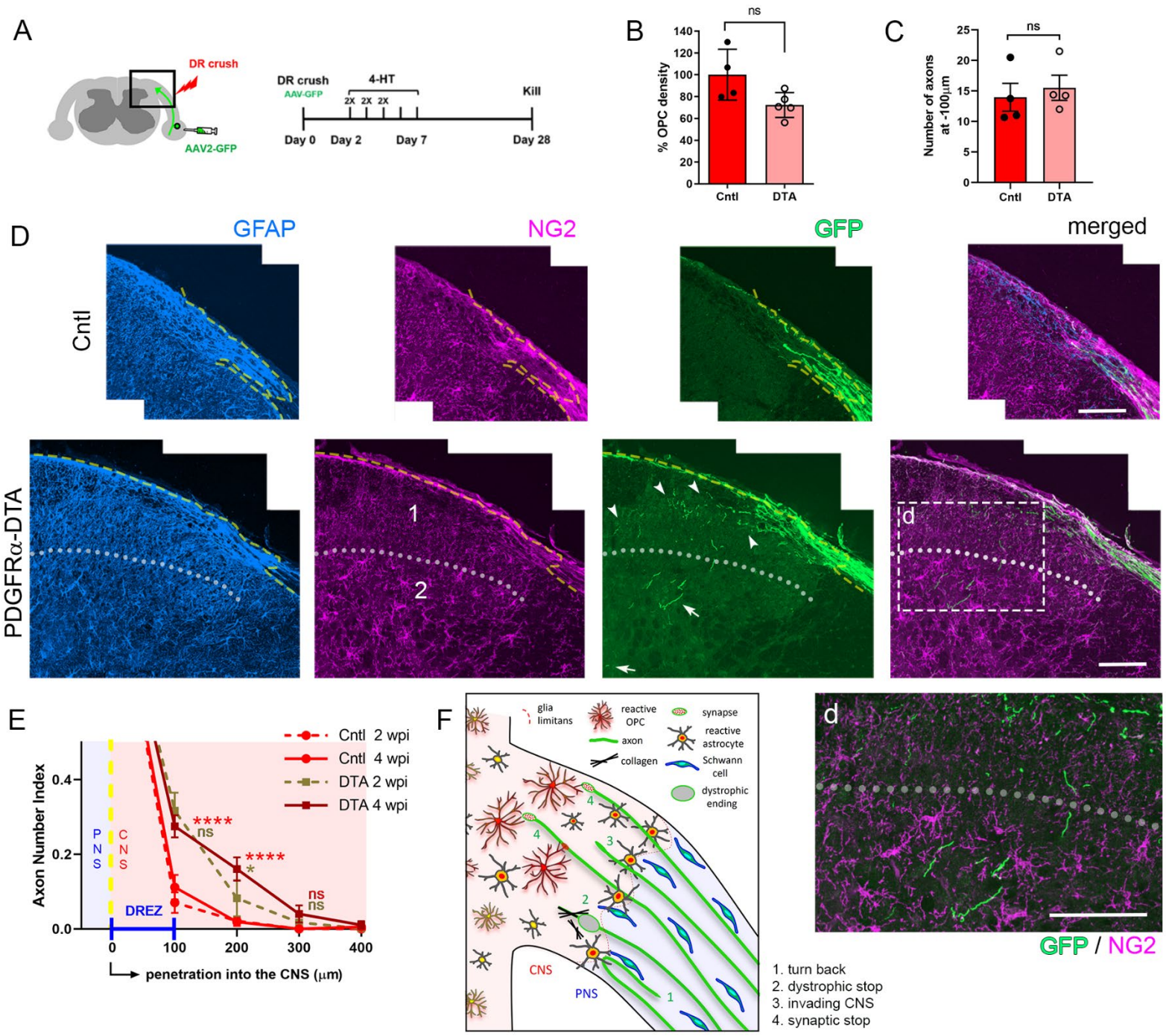


**Figure 7. Axons continue regenerating intraspinally through areas lacking OPCs**

**(A)** Diagram illustrating experimental procedures to evaluate the effects of genetic OPC ablation at 4 weeks after C5-C8 root crush followed by AAV2-GFP injections into C5 and C7 DRGs.

**(B)** Quantitative comparison of OPC density, measured by mean fluorescence intensity of NG2 staining in the spinal cord, illustrating ~30% ablation of OPCs in PDGFRα-DTA mice used for the analysis. Cntl, 100.0±23.35; DTA 72.31±11.4. Error bars represent SD. Unpaired t test (n=4 control, 5 DTA mice). ns, $p > 0.05$

**(C)** Quantification of GFP+ axons at ~100µm proximal to the borderline, illustrating insignificant difference between control and PDGFRα-DTA mice. Cntl, 13.98±2.281; DTA 15.53±2.063. Error bars represent SEM (n = 4 mice/group). Unpaired Student's t-test. ns, $p > 0.05$

**(D)** Transverse sections from a control and a PDGFRα-DTA mouse, illustrating massive repopulation of OPCs and GFP+ axons that regenerate remarkably deeply into the dorsal horn (arrows). There are noticeably fewer

OPC processes where more axons (arrowheads) regrow within the spinal cord (area 1) than where fewer axons (arrows) regenerate (area 2). Enlarged view of boxed area (d) illustrates regenerated GFP+ axons in association with repopulated OPC meshwork. Scale bar: 100μm

**(E)** Quantitative comparison of control and PDGFRα-DTA mice illustrating that ~20% axons continue to regenerate past the DREZ in DTA mice during the additional two weeks. Error bars represent SEM (n=4 mice/group). Two-way ANOVA with Sidak's multiple comparisons test. 100μm; ns, $p > 0.05$ (DTA 4 wpi vs. DTA 2 wpi); ****$p \leq 0.00001$ (DTA 4 wpi vs. control 4 wpi), 200μm; ****$p \leq 0.00001$ (DTA 4 wpi vs. control 4 wpi), *$p \leq 0.01$ (DTA 4 wpi vs. DTA 2 wpi), 300μm; ns, $p > 0.05$ (DTA 4 wpi vs. control 4 wpi, DTA 2 wpi).

**(F)** Schematic illustration of the proposed model.

See also **Figure S7**.

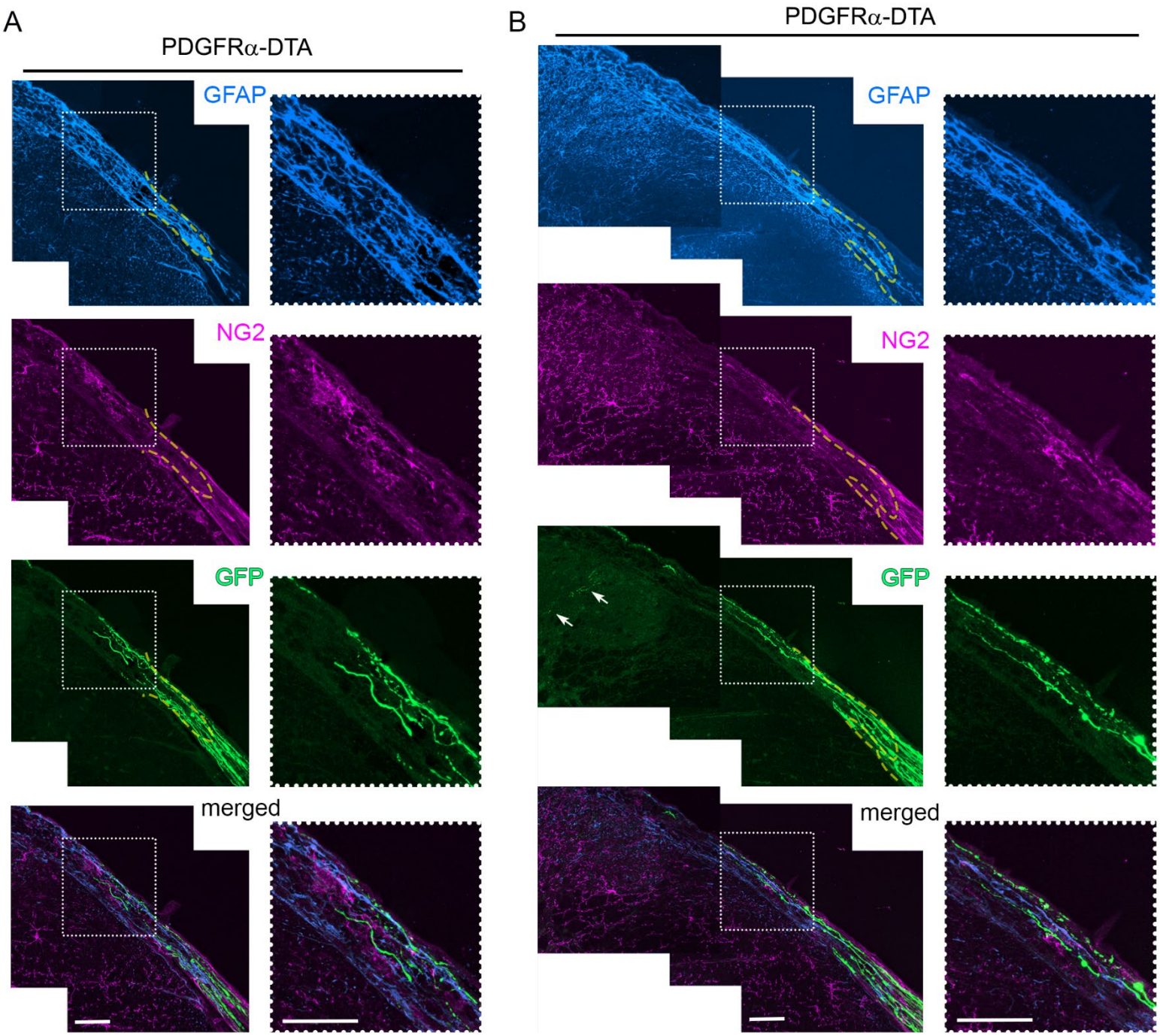


**Figure S7**. **Axons regenerate deeper into the dorsal funiculus in PDGFRα-DTA mice at 4 wpi**
**(A, B)** Two sets of transverse sections of PDGFRα-DTA mice at 4 wpi, co-labeled for GFAP and NG2, illustrating more numerous GFP+ axons (Green) that regenerated deeper into the dorsal funiculus than at 2 wpi (refer to Figure 7D). These axons terminate where OPCs are locally repopulated, in association with OPC processes (Magenta). Enlarged views of boxed area also indicate sparse distribution of OPCs where these axons regenerate. Arrows show axons reaching more deeply into the dorsal horn. Scale bar: 50μm